Hotspot *ESR1* Mutations Are Multimodal and Contextual Modulators of Breast Cancer Metastasis

Zheqi Li[1,2], Yang Wu[2,3], Megan E. Yates[2,4,5], Nilgun Tasdemir[1,2], Amir Bahreini[2,6], Jian Chen[2], Kevin M. Levine[2,7], Nolan M. Priedigkeit[1,2], Azadeh Nasrazadani[2], Simak Ali[8], Laki Buluwela[8], Spencer Arnesen[9,10], Jason Gertz[9,10], Jennifer K. Richer[11], Benjamin Troness[12], Dorraya El-Ashry[12], Qiang Zhang[13], Lorenzo Gerratana[13,14], Youbin Zhang[13], Massimo Cristofanilli[13], Maritza A. Montanez[15], Prithu Sundd[15], Callen T. Wallace[16], Simon C. Watkins[16], Caterina Fumagalli[17], Elena Guerini-Rocco[17,18], Li Zhu[19], George C. Tseng[19], Nikhil Wagle[20], Jason S. Carroll[21], Paul Jank[22], Carsten Denkert[22], Maria M. Karsten[23], Jens-Uwe Blohmer[23], Ben H. Park[24], Peter C. Lucas[7], Jennifer M. Atkinson[1,2], Adrian V. Lee[1,2,4,6], and Steffi Oesterreich[1,2,4,6,7]

ABSTRACT

Constitutively active estrogen receptor α (ER/*ESR1*) mutations have been identified in approximately one-third of ER$^+$ metastatic breast cancers. Although these mutations are known as mediators of endocrine resistance, their potential role in promoting metastatic disease has not yet been mechanistically addressed. In this study, we show the presence of *ESR1* mutations exclusively in distant but not local recurrences in five independent breast cancer cohorts. In concordance with transcriptomic profiling of *ESR1*-mutant tumors, genome-edited *ESR1* Y537S and D538G-mutant cell models exhibited a reprogrammed cell adhesive gene network via alterations in desmosome/gap junction genes and the TIMP3/MMP axis, which functionally conferred enhanced cell–cell contacts while decreasing cell-extracellular matrix adhesion. *In vivo* studies showed *ESR1*-mutant cells were associated with larger multicellular circulating tumor cell (CTC) clusters with increased compactness compared with *ESR1* wild-type CTCs. These preclinical findings translated to clinical observations, where CTC clusters were enriched in patients with *ESR1*-mutated metastatic breast cancer. Conversely, context-dependent migratory phenotypes revealed cotargeting of Wnt and ER as a vulnerability in a D538G cell model. Mechanistically, mutant *ESR1* exhibited noncanonical regulation of several metastatic pathways, including secondary transcriptional regulation and *de novo* FOXA1-driven chromatin remodeling. Collectively, these data provide evidence for *ESR1* mutation–modulated metastasis and suggest future therapeutic strategies for targeting *ESR1*-mutant breast cancer.

Significance: Context- and allele-dependent transcriptome and cistrome reprogramming in mutant *ESR1* cell models elicit diverse metastatic phenotypes related to cell adhesion and migration, which can be pharmacologically targeted in metastatic breast cancer.

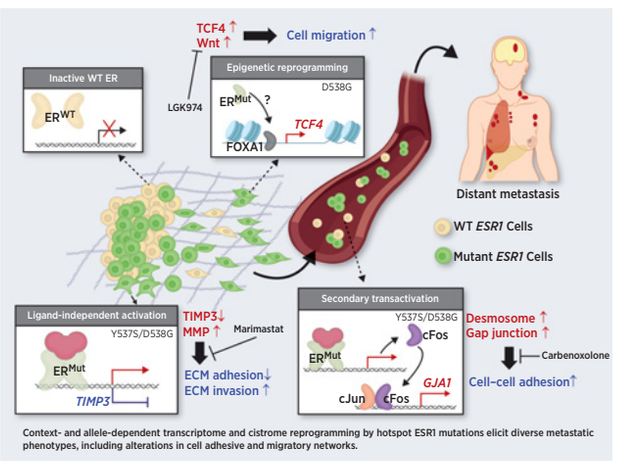

Context- and allele-dependent transcriptome and cistrome reprogramming by hotspot ESR1 mutations elicit diverse metastatic phenotypes, including alterations in cell adhesive and migratory networks.

[1]Department of Pharmacology and Chemical Biology, University of Pittsburgh, Pittsburgh, Pennsylvania. [2]Women's Cancer Research Center, Magee-Womens Research Institute, UPMC Hillman Cancer Center, Pittsburgh, Pennsylvania. [3]School of Medicine, Tsinghua University, Beijing, P.R. China. [4]Integrative Systems Biology Program, University of Pittsburgh, Pittsburgh, Pennsylvania. [5]Medical Scientist Training Program, University of Pittsburgh School of Medicine, Pittsburgh, Pennsylvania. [6]Department of Human Genetics, University of Pittsburgh, Pittsburgh, Pennsylvania. [7]Department of Pathology, University of Pittsburgh, Pittsburgh, Pennsylvania. [8]Department of Surgery and Cancer, Imperial College London, London, United Kingdom. [9]Department of Oncological Sciences, University of Utah, Salt Lake City, Utah. [10]Huntsman Cancer Institute, University of Utah, Salt Lake City, Utah. [11]Department of Pathology, University of Colorado Anschutz Medical Campus, Aurora, Colorado. [12]University of Minnesota Masonic Cancer Center, Minneapolis, Minnesota. [13]Robert H. Lurie Cancer Center of Northwestern University, Feinberg School of Medicine, Chicago, Illinois. [14]Department of Medicine (DAME) University of Udine, Udine, Italy. [15]Pittsburgh Heart, Lung and Blood Vascular Medicine Institute, University of Pittsburgh School of Medicine, Pittsburgh, Pennsylvania. [16]Center for Biological Imaging, University of Pittsburgh, Pittsburgh, Pennsylvania. [17]Division of Pathology and Laboratory Medicine, IEO, European Institute of Oncology, IRCCS, Milan, Italy. [18]Department of Oncology and Hemato-Oncology, University of Milan, Milan, Italy. [19]Department of Biostatistics, University of Pittsburgh, Pittsburgh, Pennsylvania. [20]Department of Medical Oncology and Center for Cancer Precision Medicine, Dana-Farber Cancer Institute, Harvard Medical School, Brigham and Women's Hospital, Boston, Massachusetts. [21]Cancer Research UK, Cambridge Institute, University of Cambridge, Cambridge, United Kingdom. [22]Institut of Pathology, Philipps-University Marburg, UKGM - Universitätsklinikum Marburg, Marburg, Germany. [23]Department of Gynecology with Breast Center, Charité – Universitätsmedizin Berlin, Corporate member of Freie Universität Berlin, Humbold-Univeristät zu Berlin and Berlin Institute of Health, Berlin, Germany. [24]Vanderbilt University Ingraham Cancer Center, Nashville, Tennessee.

Note: Supplementary data for this article are available at Cancer Research Online (http://cancerres.aacrjournals.org/).

Corresponding Author: Steffi Oesterreich, Department of Pharmacology and Chemical Biology, University of Pittsburgh, 204 Craft Ave #430, Pittsburgh, PA 15213. E-mail: oesterreichs@upmc.edu

Cancer Res 2022;82:1321–39

doi: 10.1158/0008-5472.CAN-21-2576

Introduction

More than 70% of breast cancers express estrogen receptor α (ER/*ESR1*). Antiestrogen therapies, including depletion of estradiol (E2) by aromatase inhibitors or antagonizing ER activity by selective ER modulators/degraders (SERM/SERD), are conventional treatments for ER^+ breast cancer. Development of resistance to these endocrine therapies, however, remains a clinical and socioeconomic challenge (1, 2).

A total of 30%–40% of endocrine-resistant metastatic breast cancer (MBC) is enriched in *ESR1* somatic bp missense mutations (3–5), that can be detected in the blood of patients with advanced disease (6, 7). Clinically, ligand-binding domain (LBD) *ESR1* mutations correlate with poor outcomes in patients with advanced disease (6, 8, 9). Recent work from our group and others has uncovered a crucial role for these *ESR1* hotspot mutations in driving constitutive ER activity and decreased sensitivity toward ER antagonists (10–12). Moreover, structural investigation of the two most frequent mutations, variants Y537S and D538G, has demonstrated that *ESR1* mutations stabilize helix 12 (H12) in an agonist conformation, thereby providing a mechanistic explanation for constitutive ER activity (13).

The identification of *ESR1* mutations in endocrine-resistant MBC suggests that mutant ER may not only mediate endocrine resistance but also have an unappreciated role in enabling metastasis. Indeed, recent *in vivo* studies showed that mutant ER can promote metastasis (14, 15), and *in vitro* studies showed a gain of cell motility (15, 16) and growth in three-dimensional culture (17). Although epithelial–mesenchymal transition (EMT) has been described as one potential explanation for the Y537S mutant (18), overall mechanisms remain largely unclear. To identify personalized therapeutic vulnerabilities in patients harboring *ESR1* hotspot mutations, there is an urgent need to decipher the mechanistic underpinnings and precise roles of mutant ER in the metastatic progression using comprehensive approaches and model systems.

Previous transcriptomic profiling performed by us and others has revealed a context dependence of *ESR1* mutation effects, as well as significant differences between the two most frequent hotspot mutations, Y537S and D538G (11, 12, 14, 15, 19). Differentially expressed genes vary widely following expression of the mutations in their respective cell line model; however, both Y537S and D538G maintain distinction from the E2-dependent wild-type (WT) ER transcriptome. Similarly, comparison of the WT and mutant ER cistromes has also revealed context-dependent and allele-specific effects on ER recruitment (11, 14). Furthermore, we recently showed that *ESR1*-mutant transcriptomic reprogramming is associated with epigenetic remodeling (19). While these findings imply that in the setting of high molecular diversity in tumors and patients, somatic *ESR1* mutations have the potential to trigger different metastatic phenotypes, this phenomenon has yet to be investigated.

In this study, we explore metastatic gain-of-function phenotypes in genome-edited *ESR1*-mutant models under the guidance of transcriptomic changes detected in clinical samples. We identify mechanisms underlying context-dependent and allele-specific metastatic phenotypes, and subsequently confirm alterations in a number of potential therapeutic targets in metastatic tumors. We believe that our systematic bedside-to-bench approach will ultimately lead to improved metastasis-free outcomes and prognosis for patients with ER^+ tumors.

Materials and Methods

Additional details and references are provided in the Supplementary Materials and Methods section.

Human tissue studies from the Women's Cancer Research Center and Charite cohorts

All patients enrolled were approved within Institutional Review Board protocols (PRO15050502) from the University of Pittsburgh (Pittsburgh, PA) and Charite Universitaetsmedizin Berlin. Informed consent was obtained from all participating patients. Biopsies were obtained and divided into distant metastatic or local recurrent tumors. Genomic DNA was isolated from formalin-fixed paraffin-embedded (FFPE) samples and *ESR1* mutation status was detected with droplet digital PCR (ddPCR) targeting Y537S/C/N and D538G mutations in preamplified *ESR1* LBD products as reported previously (7).

Circulating tumor cell analysis from the NU16B06 cohort

A retrospective cohort comprising 151 patients with metastatic breast cancer characterized for circulating tumor cells (CTC), and ctDNA at the Robert H. Lurie Comprehensive Cancer Center of Northwestern University (Chicago, IL) between 2015 and 2019 was analyzed. Patients' enrollment was performed under the Investigator Initiated Trial (IIT) NU16B06 independently from treatment line. The overall baseline staging was performed according to the investigators' choice, CTCs and ctDNA collection was performed prior to treatment start. CTC enumeration was performed though the CellSearch immunomagnetic system (Menarini Silicon Biosystems). Mutations in *ESR1* (hotspots D538 and Y537) and PIK3CA (hotspots E453 and H1047) were detected by either ddPCR assay using the QX200 ddPCR System (Bio-Rad) or through the Guardant360 high-sensitivity next-generation sequencing platform (Guardant Health). More details for CTC enumeration, mutation detection, and statistical analysis can be found in Supplementary Materials and Methods.

Cell culture

Genome-edited MCF7 (RRID: CVCL_0031) and T47D (RRID: CVCL_0553) *ESR1*-mutant cell models from different sources were maintained as described previously (11, 12, 19). Hormone deprivation was performed for all experiments, unless otherwise stated.

Reagents

17β-estradiol (E2, #E8875) was obtained from Sigma, and fulvestrant (#1047), carbenoxolone disodium (#3096), and EDTA (#2811) were purchased from Tocris. LGK974 (#14072) and T-5224 (#22904) were purchased from Cayman. Marimastat (S7156) was obtained from SelleckChem. Recombinant human Wnt3A (5036-WN-010) was purchased from R&D Systems. For knockdown experiments, siRNA against *FOXA1* (#M-010319), *DSC1* (#L-011995), *DSC2* (#L-011996), *GJA1* (#L-011042), and *GJB2* (#L-019285) were obtained from Horizon Discovery. Desmosome and scramble peptides were designed on the basis of previous studies (20, 21) and synthesized from GeneScript. Peptide sequences are presented in Supplementary Table S10.

Animal studies

Long-term metastatic evaluation

Four weeks old female *nu/nu* athymic mice were ordered from The Jackson Laboratory (002019 NU/J, RRID: IMSR_JAX:002019) according to University of Pittsburgh Institutional Animal Care and Use

Committee (IACUC)-approved protocol #19095822. MCF7- and T47D *ESR1*–mutant cells were hormone deprived and resuspended in PBS with a final concentration of 10^7 cells/mL. A total of 100 μL of cell suspension was then injected via tail vein into nude mice with 7 mice per group. Mice were under observation weekly. According to the IACUC protocol, if greater than 50% of mice in any group show predefined signs of euthanasia, the entire cohort needs to be euthanized. Cohorts were euthanized at 13 weeks for MCF7 cell-injected mice and 23 weeks for T47D cell-injected mice. Macrometastatic tumors and potential organs (lung, liver, urogenital and gastrointestinal tract) for metastatic spread were harvested. Solid macrometastatic tumors (non-lymph node) were counted for comparison. All tissues were processed for FFPE preparation and hematoxylin and eosin staining by the Histology Core at Magee-Womens Research Institute (Pittsburgh, PA). Macrometastatic tumor FFPE sections were further evaluated by a trained pathologist. Micrometastatic lesions in the lung were further examined and quantified by immunofluorescence staining as described in Supplementary Materials and Methods.

Short-term CTC cluster assessment

Four weeks old female *nu/nu* athymic mice were ordered from The Jackson Laboratory (002019 NU/J) according to University of Pittsburgh IACUC-approved protocol #19095822. MCF7 WT and mutant cells were stably labeled with RFP-luciferase by infection with the pLEX-TRC210/L2N-TurboRFP-c lentivirus plasmid. Labeled cells were hormone deprived and resuspended in PBS at a final concentration of 10^7 cells/mL. A total of 100 μL of cell suspension was then injected into nude mice with 6 mice per group via an intracardiac left ventricle injection. Postinjected mice were immediately imaged using the IVIS200 *in vivo* imaging system (124262, PerkinElmer) after D-luciferin intraperitoneal injection to confirm successful cell delivery into the circulation system. All mice were euthanized after one hour of injection and their whole blood were extracted via cardiac puncture and collected into CellSave Preservative Tubes (#790005, CellSearch). Blood samples were mixed with 7 mL of RPMI media and shipped to University of Minnesota (Minneapolis, MN) for CTC enrichment. CTCs were extracted using an electric size-based microfilter system (FaCTChekr) and stained with antibody against pan-cytokeratins (CK) and DAPI. Slides with stained CTCs were manually scanned in a blind manner and all visible single CTCs or clusters were imaged under ×5 or ×40 magnification, respectively. To set up criteria for identifying CTC clusters via images, we analyzed seven single CTCs with intact CK signal distribution and calculated the average nuclei edge to membrane distance (x). Internuclei edge distance greater than 2x for any two CTCs were excluded in CTC cluster calling. All measurements were performed in a blind manner. Details of filter and staining are included in the Supplementary Materials and Methods.

qRT-PCR

MCF7 and T47D cells were seeded in triplicates into 6-well plates with 120,000 and 90,000 cells per well, respectively. After desired treatments, RNA was and cDNA was synthesized using iScript kit (#1708890, Bio-Rad). qRT-PCR reactions were performed with Sybr-Green Supermix (#1726275, Bio-Rad), and the $\Delta\Delta C_t$ method was used to analyze relative mRNA fold changes (FC) with *RPLP0* measurements serving as the internal control. All primer sequences can be found in Supplementary Table S10.

Immunoblotting

After desired treatments, cells were lysed with RIPA buffer spiked with a fresh protease and phosphatase cocktail (Thermo Fisher Scientific, #78442) and sonicated. Protein concentrations were quantified using the Pierce BCA assay kit (Thermo Fisher Scientific, #23225). A total of 80–120 μg of protein for each sample was loaded onto SDS-PAGE gels, and then transferred onto polyvinylidene difluoride membranes. The blots were incubated with the following antibodies: desmocollin 1 (sc-398590, RRID: AB_2894905), desmoglein 2 (sc-80663, RRID: AB_2093438), plakophilin (sc-33636, RRID: AB_2164139), connexin 26 (sc-7261, RRID: AB_2110895), and cFOS (sc-52, RRID: AB_2106783) from Santa Cruz Biotechnology; ER-α (#8644, RRID: AB_2617128), HA (#3724, RRID: AB_1549585), Non-phospho-β-catenin (#19807, RRID: AB_2650576), Histone H3 (#4499, RRID: AB_10544537), AIF (#5318, RRID: AB_10634755), GSK3β (Ser9, #5558, RRID: AB_10013750), phospho-GSK3α (Ser21, #9316, RRID: AB_659836), GSK3β (#12456, RRID: AB_2636978), and GSK3α (#4337, RRID: AB_10859910) from Cell Signaling Technology; β-catenin (#610154, RRID: AB_397555) from BD Biosciences; Tubulin (T6557, RRID: AB_477584) and connexin 43 (C6219, RRID: AB_476857) from Sigma-Aldrich; and *TIMP3* (ab39184, RRID: AB_2204971) from Abcam.

IncuCyte live cell imaging system

Wound scratch assay

MCF7 or T47D cells were seeded at 150,000 cells/well into Image-lock 96-well plates (Essen Bioscience, #4379) precoated with Matrigel (Corning, #356237). Wounds were scratched in the middle of each well using a Wound Maker (Essen Bioscience, #4493). Desired treatments mixed with 5 μg/mL of proliferation blocker mitomycin C (Sigma-Aldrich, #10107409001) were loaded after two washes with PBS. The IncuCyte Zoom system was used to record wound images every 4 hours and wound closure density was calculated using the manufacturer's wound scratch assay module. For the dominant negative *TCF4* overexpression experiment, Myc-tagged DN*TCF4* plasmids (Addgene, #32729) were transiently transfected into targeted cells for a total of 24 hours before being subjected to the wound scratch assay.

Aggregation rate assay

A total of 3,000 MCF7 or 4,000 T47D cells were seeded into 96-well round bottom ultralow attachment (ULA) plates (Corning, #7007) with 100 μL of respective media in each well. Cell aggregation was monitored by the IncuCyte live cell imaging system every hour. Spheroid areas were normalized to time 0.

Calcein-labeled cell–cell interaction assay

MCF7 and T47D cells were seeded into black-walled 96-well plate at 150,000 cells per well to achieve a fully confluent monolayer after 24 hours. Separate cultures of cells were digested and labeled with 1 μmol/L calcein AM (BD Pharmingen, #564061) for 30 minutes in room temperature. A total of 40,000 labeled cells were loaded on top of the previously plated monolayers and incubated for 1 hour at 37°C. Cells were washed three times after incubation by manually pouring out the PBS washing agent. The plates were read using Victor X4 plate reader (PerkinElmer) under the excitation and emission wavelength of 485/535 nm. Cell–cell adhesion ratios were calculated by dividing the postwash readouts to the prewash readouts after each wash.

Ibidi microfluidic system

MCF7- and T47D *ESR1*–mutant cells were hormone deprived for 3 days and diluted to 10^6 cells in 14 mL of respective media before being loaded into the ibidi pump system (ibidi, #10902). Cells were constantly flowing with 15 dynes/cm of shear stress for 2 hours before immediate imaging after being seeded back into a flat bottom ULA plate. For each group, 6 wells were imaged twice. Time zero (T0) cells were also imaged as the initial timepoint control. Cell numbers in clusters or non-clusters were manually counted. Cell cluster ratios were calculated by dividing the cell numbers in clusters to the total number of cells. Cell clustering grade was calculated by the cell numbers present in each cluster. For carbenoxolone (CBX) treatment, cells were pretreated with 100 μmol/L CBX for 2 days before being added to the flow chamber. For the desmosome blocking peptides treatment, 75 μmol/L of each *DSC1*, *DSC2*, *DSG1*, and *DSG2* peptide or 150 μmol/L of each scramble peptide were premixed into cell suspension for flow experiments.

Cell extracellular matrix adhesion assay

A total of 30,000 cells/well were seeded into collagen I coated (Thermo Fisher Scientific, A1142803) or uncoated 96-well plates. For the extracellular matrix (ECM) array assay, cells were resuspended and loaded into the ECM array plate (EMD Millipore, ECM540). After a 2-hour incubation at 37°C, the plates were washed with PBS three times, and attached cells were quantified using the FluoReporter kit (Thermo Fisher Scientific, F2962). Adhesion ratios were calculated by dividing the remaining cell counts in the washed wells to the initial cell counts in prewashed plates. For *TIMP3* overexpression, the PRK5M-*TIMP3* plasmid (Addgene, #31715) was transfected into targeted cells, which was subjected to the adhesion assay after a 24-hour transfection period.

Chromatin immunoprecipitation

Chromatin immunoprecipitation (ChIP) experimentation was performed as described previously (22). The immunoprecipitation was performed using ER-α (sc543, RRID: AB_631471) and rabbit IgG (sc2027, RRID: AB_737197) antibodies (Santa Cruz Biotechnology). Histone 3 acetylation at K27 site (ab4729, RRID: AB_2218291), and Histone 3 dimethylation at K4 site (ab7766, RRID: AB_2560996) and FOXA1 (ab23738, RRID: AB_2104842) antibodies were obtained from Abcam. Detailed ChIP sequencing (ChIP-seq) analysis is provided in the Supplementary Material and Methods.

Statistical analysis

GraphPad Prism software version 7 and R version 3.6.1 were used for statistical analysis. All experimental results included biological replicates and were shown as mean ± SD, unless otherwise stated. Specific statistical tests were indicated in corresponding figure legends. All tests were conducted as two tailed, with a $P < 0.05$ considered statistically significant. Drug synergy was calculated on the basis of the Bliss independence model using the SynergyFinder (https://synergyfinder.fimm.fi/; ref. 23). Bliss synergy scores were used to determine synergistic effects.

Data availability statement

The ER and FOXA1 ChIP-seq data have been deposited onto the Gene Expression Omnibus database (GSE125117 and GSE165280). All publicly available resources used in this study are summarized in Supplementary Table S11. All raw data and scripts are available upon request from the corresponding author.

Results

Significant enrichment of *ESR1* mutations in distant metastases compared with local recurrences

We compared *ESR1* mutation frequencies between distant metastatic and locally recurrent tumors. A combination of four previously reported clinical cohorts (MSKCC, METAMORPH, POG570, and IEO) showed that while 155 of 877 distant metastases (18%) harbored *ESR1* mutations, none were found in 44 local recurrences (**Table 1**; Supplementary Table S1; refs. 24–27). To expand upon this observation, we additionally screened 75 ER^+ recurrent tumors from the Women's Cancer Research Center (WCRC) and Charite Hospital for *ESR1* hotspot (Y537S/C/N and D538G) mutations using highly sensitive ddPCR. We identified 12 *ESR1* mutation–positive cases among the distant metastases (25%), whereas none of the local recurrences were *ESR1* mutation positive (**Table 1**; Supplementary Table S2). There was no significant difference in time to recurrence for patients with distant versus local recurrences (Supplementary Fig. S1A; Supplementary Table S3), making it less likely that the observed differences could simply be due to duration of time to recurrence between local and distant recurrences, as was suggested previously (6). If however, we compare time with distant recurrence between tumors with WT and mutant *ESR1*, we observed significantly longer time to recurrence in two of the five cohorts (Supplementary Fig S1B). For three of the cohorts (WCRC/Charite, POG570, and MSKCC), details on lines of therapies was available, and we observed that in two of the cohorts, patients with distant metastases had on average significantly more lines of therapy compared with those with local recurrences (Supplementary Fig. S1C and S1D), and that patients with *ESR1*-mutant tumors had been exposed to more lines of therapies than those with WT tumors (Supplementary Fig. S1E). Finally, we repeated our comparative analysis of frequency of *ESR1* mutations in local and distant recurrences restricting it to patients exposed to endocrine therapies and confirmed significant enrichment of *ESR1* mutations in distant metastasis (Supplementary Table S1). Thus, while collectively these analyses recapitulated that *ESR1* mutations are arising primarily as an outcome of therapeutic selection, their more frequent occurrences in distant compared with local recurrences suggest a potential role in promoting metastasis in addition to conferring endocrine resistance.

ESR1-mutant tumors show a unique transcriptome associated with multiple metastatic pathways

To identify candidate functional pathways mediating the metastatic properties of *ESR1*-mutant cells, we compared WT and *ESR1*-mutant tumor transcriptomes from four cohorts of ER^+ metastatic tumors: our local WCRC cohort (46 *ESR1* WT and eight mutant tumors; refs. 28–30) and three previously reported cohorts—MET500 (34 *ESR1* WT and 12 mutant tumors), POG570 (68 *ESR1* WT and 18 mutant tumors), and Dana-Farber Cancer Institute (DFCI; 98 *ESR1* WT and 32 mutant tumors; refs. 14, 27, 31; **Fig. 1A**; Supplementary Table S4).

Although principal component analyses (PCA) on global transcriptomes did not segregate *ESR1* WT and mutant tumors (Supplementary Fig. S2A), both "Estrogen Response Early" and "Estrogen Response Late" signatures were significantly enriched in *ESR1*-mutant tumors in three of four cohorts, with a trend toward enrichment in the fourth cohort (**Fig. 1B**). These results recapitulate the observation of ER hyperactivation as a result of hotspot mutations, previously described

Table 1. Significant enrichment of *ESR1* mutations in distant compared with local recurrences.

Cohorts	Site of recurrence	Total number	*ESR1* WT	*ESR1* Mutant	Fisher Exact *P*
METAMORPH/ POG570/ MSKCC/IEO Merged	Distant	877	722 (82%)	155 (18%)	0.0006
	Local	44	44 (100%)	0 (0%)	
WCRC/Charite	Distant	48	36 (75%)	12 (25%)	0.0031
	Local	27	27 (100%)	0 (0%)	

Note: Top panel: Data from 877 distant metastatic and 44 local recurrence cases were merged from three cohorts (METAMORPH, 39 distant/9 local; POG570, 86 distant/14 local; MSKCC, 716 distant/8 local; IEO, 36 distant/13 local). *ESR1* mutation status was previously identified by whole-exome sequencing (METAMORPH), whole genome sequencing (POG570), or target panel DNA sequencing (MSKCC, IEO). Bottom panel: Forty-eight distant ER-positive metastases and 27 local ER-positive recurrences were obtained from the WCRC and Charite cohorts. Genomic DNA (gDNA) was isolated from either FFPE or frozen tumor tissues and subjected to ddPCR detection with specific probes against Y537S, Y537C, Y537N, and D538G hotspot point mutations (cDNA rather than gDNA was used for three of the local recurrent samples). Hotspot *ESR1* mutation incidences between distant metastatic and local recurrent samples in both panels were compared using a Fisher exact test.

in other preclinical studies (11, 12, 14). Differential gene expression analysis identified a considerable number of altered genes that were associated with *ESR1* mutations (**Fig. 1C**; Supplementary Table S5), which further inferred functional alterations in various metastasis-related pathways. Remarkably, "Cell-To-Cell Signaling & Interaction" and "Cell Movement" were featured among the top five altered pathways for *ESR1*-mutant tumors in all four cohorts (**Fig. 1D**).

In addition to the broad effects associated with *ESR1* mutations, we next questioned whether different *ESR1*-mutant variants could display divergent functions. A meta-analysis of the five above-mentioned ER^+ MBC cohorts examining *ESR1* mutations underscored D538G (37%) and Y537S (24%) as the predominant variants (**Fig. 1E**). Given the challenge of merging RNA sequencing (RNA-seq) datasets from multiple cohorts due to immense technical variations, we selectively compared mutation variant-specific transcriptomes of 10 Y537S- or eight D538G-harboring tumors with the WT counterpart ($n = 32$), respectively, from the DFCI cohort, which provided the largest numbers and thus maximized statistical power. Aligning enrichment levels of 50 hallmark gene sets for the two mutant variants again confirmed "Estrogen Response Early" and "Estrogen Response Late" as the top co-upregulated pathways (**Fig. 1F**), with Y537S tumors displaying higher ER activation (Supplementary Fig. S2B), consistent with cell line studies (12, 32). The similar observation was also validated in MET500 and POG570 cohort regardless of the smaller sample size (Supplementary Fig. S2B). We also identified enriched cell cycle–related pathways (E2F targets, G_2–M checkpoint, and mitotic spindle) and metabolic-related pathways (fatty acid, bile acid, and xenobiotic metabolisms) in Y537S and D538G tumors, respectively, implying that different *ESR1*-mutant variants might hijack distinct cellular functions to promote malignancy. Again, similar trends of these mutant-variant pathways were recapitulated in POG570 cohort (Supplementary Fig. S2C). Taken together, these results provide support that despite mutant variant-specific alterations, *ESR1* mutations might broadly mediate metastatic phenotypes through effects on cell-to-cell interactions and cell movement. We next validated the *in silico* results using previously established genome-edited MCF7 and T47D cell line models (12).

ESR1-mutant cells exhibit stronger cell–cell adhesion

We first addressed the enrichment of cell–cell interaction signaling in the mutant tumors through morphologic inspection of cell cluster formation in suspension culture (**Fig. 2A**). We observed more compact cell clusters in MCF7- and T47D-mutant cell lines compared with their WT counterparts after 6 days of suspension culture. A time course study confirmed enhanced cluster formation 24–48 hours past cell seeding (Supplementary Fig. S3A). Similar observations were made in individual clones, eliminating the possibility for clonal effects (Supplementary Fig. S3B).

Because *ESR1*-mutant cells displayed significantly increased ligand-independent growth in suspension (**Fig. 2B**), we sought to rule out the possibility that increased cluster formation was simply a result of increased cell number by assessing cell–cell adhesive capacity using multiple approaches in short-term culture (within 1 day). We therefore directly quantified homotypic cell–cell interactions by measuring the adhesion of calcein-labeled *ESR1* WT or mutant cells. This assay showed that both MCF7-mutant cells exhibited significantly stronger cell–cell adhesion compared with the WT cells (**Fig. 2C**). In T47D cells, a similar effect was observed, but was limited to the T47D-Y537S–mutant cells (Supplementary Fig. S4A). These assays were complemented by quantification of cell aggregation rates as a direct reflection of cell–cell adhesion, which confirmed faster aggregation in MCF7-Y537S/D538G and T47D-Y537S cells (**Fig. 2D**; Supplementary Fig. S4B–S4D). In addition, these stronger cell–cell adhesive properties were also reproduced in additional *ESR1*-mutant cell models from other laboratories (Supplementary Fig. S4E and S4F; refs. 11, 19).

Cell–cell interaction has been reported to affect several stages of metastasis, including collective invasion, intravasation, dissemination, and circulation (33–35). To test whether ER mutations may affect tumor cell–cell adhesion in circulation, we utilized a microfluidic pump system to mimic arterial shear stress. Comparing representative images before and after 2 hours of microfluidic flow, we found MCF7 *ESR1*-mutant cells had a greater tendency to aggregate together (**Fig. 2E** and **F**). Larger clusters comprised of five or greater cells were more prevalent in the *ESR1*-mutant cell lines, whereas smaller two-cell clusters were diminished (**Fig. 2G**). A similar phenotype was also identified in additional MCF7 *ESR1*-mutant cells and in our T47D-Y537S cell line (Supplementary Fig. S5A–S5I), consistent with our observations in static conditions. In an additional orthogonal approach, we utilized a quantitative microfluidic fluorescence microscope system simulating blood flow (36). Quantification of dynamic adhesion events normalized to adhesion surfaces revealed a consistent enhanced cell–cell adhesion capacity of *ESR1*-mutant MCF7 cells (Supplementary Fig. S5J and S5K; Supplementary Videos S1–S3). Together, these results show that hotspot *ESR1* mutations confer increased cell–cell attachment under static and fluidic conditions, and that the effect size is dependent upon mutation type and genetic backgrounds. These findings are at odds with increased EMT features (18), and indeed the majority of *ESR1*-mutant models and tumors did not show increased EMT signature or increased expression of EMT marker genes (Supplementary Fig. S6A–S6D).

We next sought to assess whether this unexpected phenotype translated into numbers of CTC clusters and subsequent metastasis *in vivo*. One hour after intracardiac injection into athymic mice, circulating MCF7 WT and mutant cells were enriched from blood using a previously described electrical CTC filtering method (**Fig. 2H**; ref. 37). A total of 41%–81% of CTC clusters were composed of both

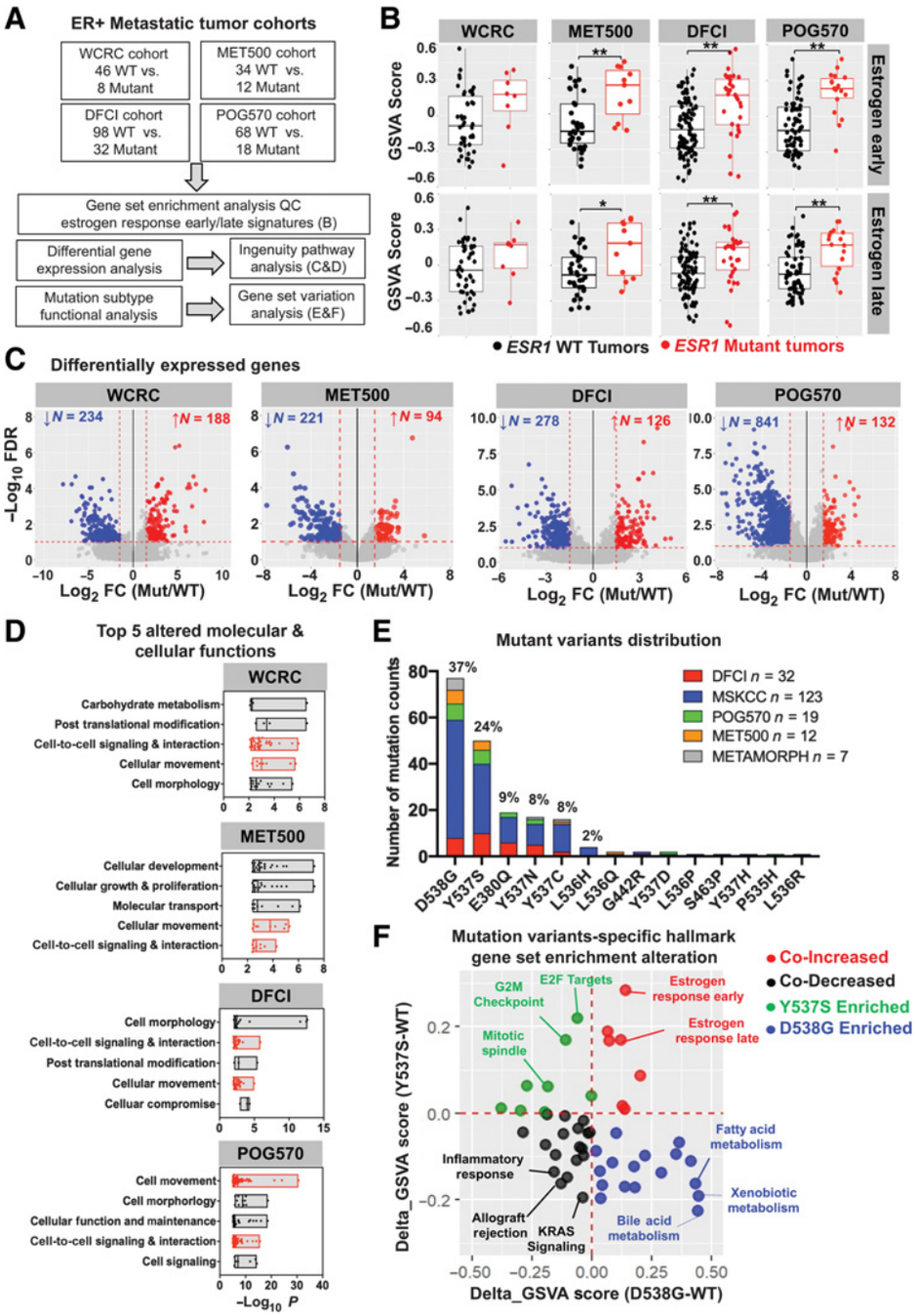

Figure 1.

Transcriptomic landscape of *ESR1*-mutant MBCs. **A,** Schematic overview of transcriptomic analysis of four ER$^+$ MBC cohorts. **B,** Box plots representing the enrichment levels of "Estrogen Response Early" and "Estrogen Response Late" signatures in *ESR1*-mutant versus *ESR1* WT metastatic tumors in each cohort (WCRC, 46 *ESR1* WT/8 mutant; MET500, 34 *ESR1* WT/12 *ESR1* mutant; DFCI, 98 *ESR1* WT/32 mutant; POG570, 68 *ESR1* WT/18 mutant). Four quantiles are shown in each plot. Mann–Whitney *U* test was used to compare the enrichment of the signatures in WT and mutant tumors. *, $P < 0.05$; **, $P < 0.01$. **C,** Volcano plots representing the differentially expressing genes in *ESR1*-mutant tumors versus WT tumors in the three MBC cohorts. Differentially expressing genes were selected using the cutoff of FDR < 0.1 and $|\log_2 FC| > 1.5$. Genes that were upregulated or downregulated are labeled in red and blue, respectively, with corresponding counts. **D,** Dot plots showing the top five altered cellular and molecular functional categories derived from differentially expressing genes analysis using Ingenuity Pathway Analysis software. Specific subfunctions within overarching categories are presented as individual dots. Consistently altered pathways across all four cohorts are indicated in red. **E,** Stacked bar plot showing the distribution of 14 hotspot *ESR1* mutations identified in six independent cohorts using unbiased DNA sequencing approaches. Specific sample numbers are indicated in the plots. Variants with percentages above 1% are labeled on the top of each bar. **F,** Scatter plot representing enrichment level distribution of 50 hallmark gene sets in 10 Y537S and eight D538G metastatic tumors (after being normalized against 98 WT counter parts) from the DFCI cohort. Top enriched pathways from each quartile are labeled.

cancer and non-cancer cells (Supplementary Fig. S7A). Despite no difference in the average amount of single CTCs and CTC clusters per mouse between the WT and mutant *ESR1* (Supplementary Fig. S7B and S7C), we found that overall MCF7-Y537S–mutant cells were significantly enriched in clusters with greater than two cells (**Fig. 2I**). Furthermore, quantification of internuclei distances between two-cell clusters revealed denser MCF7-Y537S clusters (**Fig. 2J**), supporting stronger MCF7-Y537S cell–cell interactions in an *in vivo* blood circulation environment. The data from the MCF7-D538G–mutant cells did not recapitulate the adhesive phenotype we discerned *in vitro*, suggesting mutation site-specific interactions with the *in vivo* microenvironment potentially affect cluster formation.

We next performed tail vein injection and monitored bloodborne metastatic development in longer term *in vivo* experiments without estradiol supplement (**Fig. 2K**). We observed multiple distant macrometastatic tumors in 4 of 6 (67%) MCF7-Y537S mutant cell-injected mice (**Fig. 2L**), likely as an outcome of the well-established ligand-independent cell growth. In contrast, distant macrometastatic tumor was observed in only one mouse of MCF7-D538G group (1/7) and none in MCF7-WT group (0/7; **Fig. 2M**, left). The enhanced macrometastasis observed in MCF7-Y537S but not D538G mutant was consistent with our *in vivo* CTC clustering experiment, opening up the possibility that the enhanced CTC clustering ability might confer an additional metastatic advantage. We detected no difference in lung micrometastatic foci areas between WT and mutant cell-injected mice, potentially due to a high baseline of MCF7 lung colonization capacity (**Fig. 2M**, right). In contrast to our results with MCF7 cells, we only discerned one macrometastatic tumor from each T47D-mutant group (Y537S: 1/6; D538G: 1/7) and none in T47D-WT group (0/7) after 23 weeks of injection (**Fig. 2O**, left), underpinning its less aggressive behavior as compared with MCF7 cells (38, 39). However, both T47D-Y537S– and T47D-D538G–mutant cells resulted in enlarged lung micrometastases (**Fig. 2N** and **O**, right).

Encouraged by our *in vitro* and *in vivo* findings, we next examined CTC clusters in patients with *ESR1*-mutant tumors. Taking advantage of a recent CTC sequencing study (40), we sought to generate CTC cluster gene signatures. Differential gene expression analysis in 2 patients with ER^+ disease who had at least two CTC clusters and single CTCs sequenced identified CTC cluster enriched genes (Supplementary Fig. S8A; Supplementary Table S6), which we subsequently applied to our RNA-seq dataset with 51 pairs of ER^+ primary-matched metastatic tumors (44 *ESR1* WT and seven mutant) merged from the WCRC and DFCI cohorts. *ESR1*-mutant metastatic tumors exhibited significantly higher enrichment of CTC cluster-derived gene signatures (Supplementary Fig. S8B and S8C).

To examine the interplay between *ESR1* mutations, numbers of CTCs, and clinical outcome, we analyzed a cohort of 151 patients with MBC. Median age at the first blood draw for CTCs enumeration was 55 years [interquartile range (IQR): 44–63 years], 76 patients (50.3%) were diagnosed with ER^+ HER2-negative MBC, 38 (25.2%) with HER2-positive MBC and 37 (24.5%) with triple-negative breast cancer. Bone (49.7%), lymph nodes (41.1%), lung (34.4%), and liver (34%) were the most common sites of metastasis (Supplementary Table S7). Median number of CTCs was 1 (IQR: 0–10), clusters were detectable in 14 patients (9.3%; **Fig. 2P**) and in this subgroup the median number of clustered CTCs (i.e., number of CTCs involved in clusters) was 15.5 (IQR: 4–20). Clusters with CTCs >4 and ≤4 were detected in 10 (6.6%), and 4 (2.7%) cases, respectively. Among patients without clusters (90.7%), 101 (66.89%), and 36 (23.84%) were respectively classified as stage IV indolent (<5 CTCs) and aggressive (≥5 CTCs) according to our previous study (Supplementary Table S7; ref. 41). Mutations in hotspots D538 and Y537 of *ESR1* were detected in 30 patients (19.9%), while mutations in hotspots E453 and H1047 of PIK3CA were detected in 40 patients (26.5%; Supplementary Table S7). Median follow-up was 30.8 months. A significant association was observed between *ESR1* genotype status and clustered CTCs > 4 ($P = 0.029$; **Fig. 2Q**), a significant association was retained after adjusting for MBC subtype [OR: 5.51, 95% confidence interval (CI): 1.29–23.52, $P = 0.021$]. A similar trend was highlighted in the ER^+ HER2-negative subgroup specifically (Supplementary Fig. S8D). No association was observed with respect to PIK3CA ($P = 0.725$). Notably, patients with > 4 clustered CTCs experienced the worse prognosis with respect to stage IV indolent in terms of overall survival (OS) both in the general population (**Fig. 2R**; $P < 0.0001$) and in the ER^+ HER2-negative subgroup (Supplementary Fig. S8E; $P < 0.0001$). After adjusting for MBC subtype, >4 clustered CTCs and Stage IV aggressive without clusters retained their prognostic impact (respectively, HR: 15.50, 95% CI: 6.90–34.82, $P < 0.001$; HR: 2.37, 95% CI: 1.38–4.06, $P = 0.002$).

Mutant *ESR1* cells show increased desmosome gene and gap junction gene families

To elucidate the mechanism of enhanced cell–cell adhesion, we investigated the enrichment of four major cell–cell junction subtypes—desmosomes, gap junctions (connexons), tight junctions, and adherens junctions within the cell model RNA-seq data (Supplementary Table S6; ref. 12). Enrichment of the desmosome gene and gap junction gene families was observed in both MCF7-Y537S/D538G and T47D-Y537S cells (**Fig. 3A**). Tight junctions were enriched in WT cells, and there were no differences in the adherens junction gene family expression (Supplementary Fig. S9A). Individual gene expression analysis (FC > 1.2, $P < 0.05$) identified 18 commonly upregulated desmosome genes and four gap junction genes in both MCF7 *ESR1*-mutant cell lines (**Fig. 3B**). In addition to keratins, induction of classical desmosome genes *DSC1/2*, *DSG1/2*, and *PKP1*, and gap junction genes *GJA1, GJB2*, and *GJB5* were observed and validated by qRT-PCR in MCF7 cells (**Fig. 3D**). Higher protein levels were also observed for *DSC1*, *DSG2*, *PKP1*, *GJA1* (Cx43), and *GJB2* (Cx26; **Fig. 3C**). Immunofluorescence staining revealed significantly higher *DSG2* expression in MCF7-Y537S at cell–cell contact surfaces, with a trend observed in MCF7-D538G (**Fig. 3E**). Consistent with the weaker *in vitro* cell–cell adhesion phenotypes in T47D-mutant cells, we observed less pronounced desmosome and gap junction gene expression changes in T47D-Y537S cells (Supplementary Fig. S9B). We validated the overexpression of the key desmosome and gap junction genes in RNA-seq datasets from seven additional *ESR1*-mutant cell models and performed further validation studies in two of them (Supplementary Fig. S9C–S9E; refs. 11, 15, 19). Moreover, mining RNA-seq data from recently reported *ESR1* WT and mutant *ex vivo* CTC models (42), we observed overexpression of three gap junction and desmosome genes in the *ESR1*-mutant CTC lines (Supplementary Fig. S9F). Finally, the top upregulated desmosome and gap junction genes (Supplementary Table S6) were also found significantly enriched in intrapatient matched primary and metastatic lesions with *ESR1* mutations (**Fig. 3F**).

We next investigated the functional roles of the reprogrammed adhesome in the *ESR1*-mutant MCF7 cells. Transient individual knockdown of *DSC1*, *DSC2*, *GJA1*, *or GJB2* did not cause significant changes in adhesion in either *ESR1*-mutant line (Supplementary Fig. S10A). However, we found compensatory effects observed in the desmosome and gap junction knockdowns as exemplified by increased

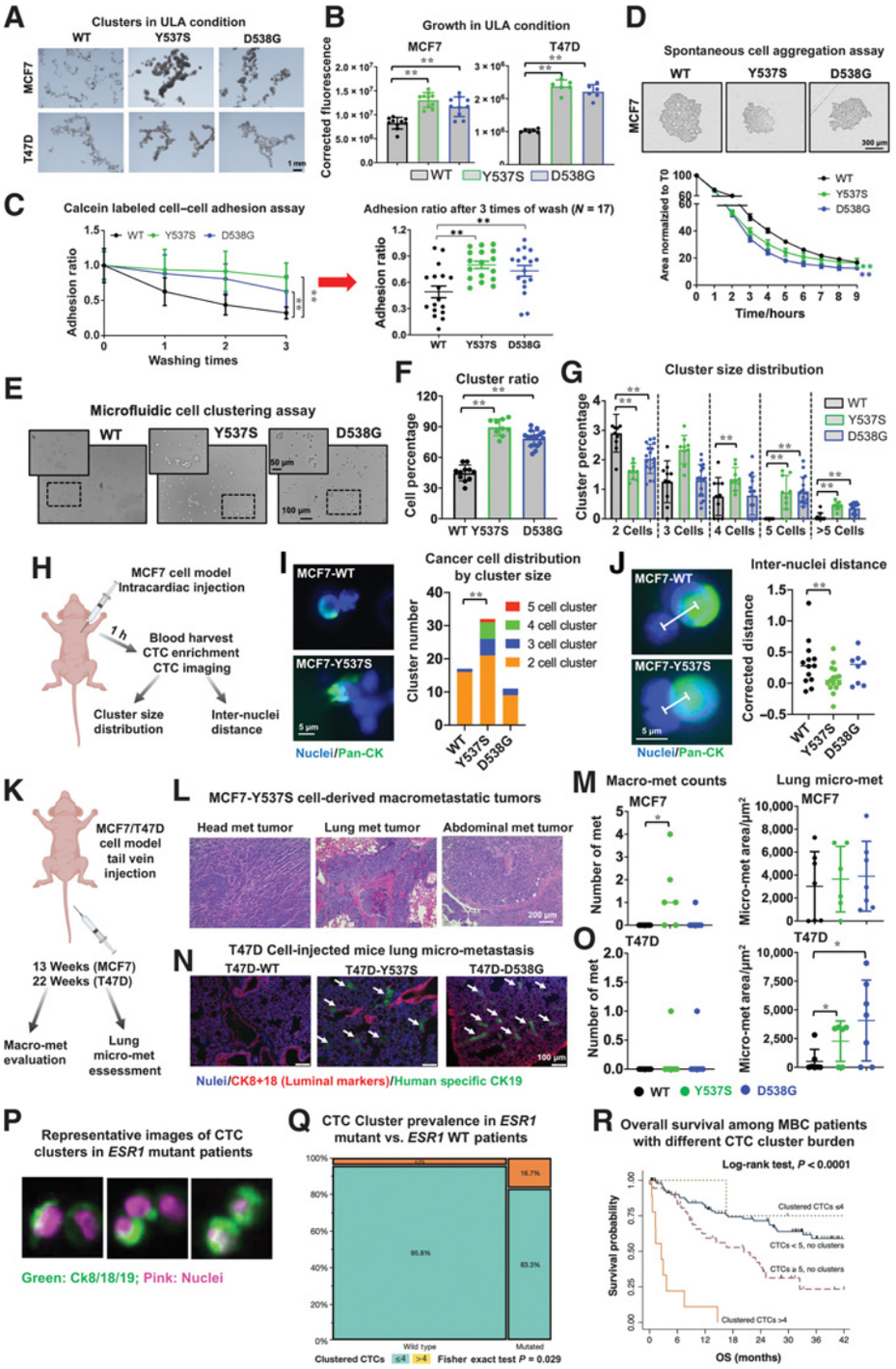

Figure 2.

ESR1-mutant cells exhibit stronger cell–cell adhesion. **A,** Representative images of day 6 hormone-deprived MCF7 and T47D spheroids seeded in 6-well ULA plates. Images were taken under ×1.25 magnification. Representative experiment from three independent repeats is shown. **B,** Bar plot representing day 7 cell numbers of MCF7 or T47D WT and *ESR1*-mutant cells seeded into flat bottom ULA plates. Cell abundance was quantified using CellTiter Glo. Fluorescence readouts were corrected to background measurements. Each bar represents mean ± SD, with 10 (MCF7) or 6 (T47D) biological replicates. Representative experiment from six independent repeats is shown. Dunnett test was used between WT and each mutant. **, $P < 0.01$. **C,** Left, a calcein-labeled cell–cell adhesion assay was performed in MCF7 WT and mutant cells. Adhesion ratios were calculated by dividing the remaining cells after each wash to the initial readout from unwashed wells. A pairwise two-way ANOVA between WT and each mutant was utilized. Each point represents mean ± SD with five biological replicates. Representative experiment from 17 independent repeats is shown. Right, adhesion ratios after three washes were extracted from 17 independent experiments displayed as mean ± SEM. Dunnett test was used to compare between WT and each mutant. **, $P < 0.01$. (*Continued on the following page.*)

GJA1 levels after *DSC1* or *DSC2* knockdown (Supplementary Fig. S10B). The adhesive phenotype was disrupted, however, with an irreversible pan-gap junction inhibitor, CBX, or with blocking peptide cocktails against desmocollin1/2 and desmoglein1/2 proteins. Both treatments caused significant inhibition of cell–cell aggregation in static conditions (Supplementary Fig. S10C and S10D) as well as diminished cluster propensities and size in microfluidic conditions (**Fig. 3G–L**), suggesting redundancy in the mutant-driven reprogrammed desmosome and connexon pathways. In summary, MCF7-Y537S/D538G and T47D-Y537S mutants showed increased expression of desmosome and gap junction gene family components, which contributes to our observed enhanced cell–cell adhesion phenotype.

We next investigated the mechanisms underlying the elevated desmosome and gap junction components in *ESR1*-mutant cells. Because hotspot *ESR1* LBD mutations are well described as conferring constitutive ER activation, we first examined whether these cell–cell adhesion target genes are direct outcomes of ligand-independent transcriptional programming. Interrogating publicly available RNA-seq and microarray datasets of six estrogen-treated ER^+ breast cancer cell lines (12, 22, 43, 44), we found limited and inconsistent E2 induction of all examined cell–cell adhesion genes when compared with classical E2 downstream targets such as *GREB1* and *TFF1* (Supplementary Fig. S11A). Surprisingly, mining our MCF7 *ESR1*-mutant cell model ER ChIP-seq data (45) showed an absence of proximate Y537S- or D538G-mutant ER binding sites [±50 kb of transcription start site (TSS)] at desmosome and connexon target gene loci. These results suggest that the reprogrammed cell–cell adhesome is not a direct consequence of mutant ER genomic binding.

We therefore hypothesized that these altered adhesion target genes might be regulated via a secondary downstream effect of the hyperactive mutant ER. A 7-day siRNA ER knockdown assessment identified *GJA1* as the only target gene that could be blocked in mutant cells following ER depletion, whereas, strikingly, *DSC1*, *DSG1*, *GJB2*, and *GJB5* mRNA levels were increased in all cell lines (**Fig. 3M**). This was congruent with *ESR1* knockdown in five additional ER^+ parental cell lines, with the majority exhibiting a decrease in *GJA1* expression levels (Supplementary Fig. S11B). To unravel potential intermediate transcription factors (TF) involved in the secondary regulation, we examined the levels of TFs previously reported to regulate *GJA1* expression (Supplementary Fig. S11C; ref. 46). Among those, the AP1 family component *FOS* (cFOS) was identified as the top TF upregulated in *ESR1*-mutant cells in a ligand-independent manner. In addition, the AP1-associated transcriptional signature was also significantly enriched in MCF7 *ESR1*-mutant cells (Supplementary Fig. S11D), and hence we tested whether *GJA1* overexpression was dependent on the cFOS/AP1 transcriptional network. Higher cFOS mRNA and protein levels in *ESR1*-mutant cells were confirmed, which declined along with *GJA1* levels after *ESR1* knockdown (**Fig. 3N**; Supplementary Fig. S11E). Importantly, pharmacologic inhibition of cFOS-DNA binding partially rescued *GJA1* overexpression in *ESR1*-mutant cells (**Fig. 3O**; Supplementary Fig. S11F–S11G). In conclusion, our results denote *GJA1* as an indirect target of mutant ER through activation of the cFOS/AP1 transcriptional axis in MCF7 cell models.

Because the majority of the cell–cell adhesion targets altered in the *ESR1*-mutant cells were not direct ER target genes (Supplementary Fig. S11A and S11B), we investigated potential impacts of epigenetic remodeling on these targets. Using our recently reported assay for transposase-accessible chromatin using sequencing (ATAC-seq) dataset from T47D *ESR1*-mutant cells (19), we observed that one of the connexon targets, *GJB5*, exhibited increased chromatin accessibility at its gene locus in T47D-Y537S cells (Supplementary Fig. S12A and

(*Continued.*) **D,** Line plot representing the aggregation ratio of MCF7 cells seeded into round bottom ULA plates. Cell aggregation processes were followed by the IncuCyte live cell imaging system every hour. Spheroid areas were normalized to time 0. Each dot represents mean ± SD, with eight biological replicates. Representative images after 3 hours of aggregation are shown across the top. Images were captured under ×10 magnification. Representative experiment from five independent repeats is shown. A pairwise two-way ANOVA between WT and each mutant was utilized. **, $P < 0.01$. **E,** Representative images of MCF7 cell cluster status after 2 hours of flow under physiologic shear stress produced by the ibidi microfluidic system. Images were taken under ×10 magnification. A regional 2× zoom in is presented on the top of each image. Representative experiment from three independent repeats is shown. **F,** Bar graph representing the percentage of MCF7 cells in a cluster based on the quantification of cluster and single-cell numbers from 12 representative images per group. Each bar represents mean ± SD. Cell cluster ratios after 2 hours of flow were further normalized to time 0 to correct for baseline preexisting clusters. Representative experiment from three independent repeats is shown. Dunnett test was used between WT and mutant cells. **, $P < 0.01$. **G,** Bar plots showing the cluster size distribution of MCF7 cells after normalization to time 0. Each bar represents mean ± SD from 12 representative images per group. Representative experiment from three independent repeats is shown. Dunnett test was used between WT and each mutant cell type within the same cluster size category. **, $P < 0.01$. **H,** Schematic overview of short-term *in vivo* circulating tumor cell evaluation experimental procedure. **I,** Left, representative images of two-cell clusters (WT) and a multicellular cluster (Y537S). Images were taken under ×40 magnification. Right, stacked bar chart representing the distribution of cancer cells in each cluster type. This experiment was performed once. Fisher exact test was applied to test whether multicellular clusters were enriched in *ESR1*-mutant cells. **, $P < 0.01$. **J,** Left, representative images of a WT and Y537S two-cell cluster. Lines connecting the two nuclei centers were indicated. Images were taken under ×40 magnification. Right, dot plot represents the internuclei distance of all two-cell clusters in MCF7 WT and mutant cells. Measured distances were normalized to the average radius of both cells of this cluster size to avoid cell size bias. This experiment was performed once. Mann–Whitney *U* test was performed between WT and each mutant cell. **, $P < 0.01$. **K,** Schematic overview of *in vivo* metastatic evaluation of *ESR1*-mutant cells introduced via tail vein injections. **L,** Representative hematoxylin and eosin staining images showing the tumorous portion of MCF7-Y537S–induced macrometastatic (macro-met) tumors from three different mice. This experiment was performed once. Images were taken under ×20 magnification. **M,** Left, dot plots showing the number of macrometastatic per mouse from MCF7 *ESR1* WT and mutant cell–injected mice. Pairwise Mann–Whitney *U* test was used to compare the macrometastatic numbers in each mutant group to WT cell–injected groups. Right, quantification of lung micrometastatic (micro-met) areas based on human-specific CK19 staining quantification. This experiment was performed once. Pairwise Mann–Whitney *U* test was applied for statistical analysis (WT, $n = 7$; Y537S, $n = 6$; D538G, $n = 7$; *, $P < 0.05$). **N,** Representative images of micrometastatic loci on the lung sections of T47D-*ESR1*–mutant cell–injected mice. Images were taken under ×10 magnification. White arrow, metastatic loci. This experiment was performed once (WT, $n = 7$; Y537S, $n = 6$; D538G, $n = 7$; blue, nuclei; red, CK8+18; green, human-specific CK19). **O,** Left, dot plots showing the macrometastatic counts per mouse from T47D *ESR1* mutant–injected mice. Pairwise Mann–Whitney *U* test was used to compare the macro-met numbers in each mutant group to WT cell-injected groups. Right: Quantification of lung micro-met areas based on CK19 staining and was performed in a blind manner. This experiment was performed once. Pairwise Mann–Whitney *U* test was applied for statistical analysis ($N = 1$; *, $P < 0.05$). **P,** Representative images of CTC clusters detected through the CellSearch Platform after EpCAM-dependent enrichment (pink, nuclei; green, CK8/CK18/CK 19). Image resolution and magnification were achieved in accordance with the CellSearch Platform. **Q,** Mosaic plot showing the association between *ESR1* genotype status and clustered CTCs. A significant positive association was observed by Fisher exact test between *ESR1* mutations and high clustered CTCs (clustered CTCs > 4). **R,** Kaplan–Meier plot representing the impact of clustered CTCs in terms of OS. Patients with clustered CTCs > 4 experienced the worse prognosis in terms of OS both with respect to those without clusters (both stage IV indolent and stage IV aggressive) and those with clusters but with ≤ 4 clustered CTCs ($P < 0.0001$). Patients at risk are reported at each time point. Log-rank test was to compare the survival curves of the two patient subsets.

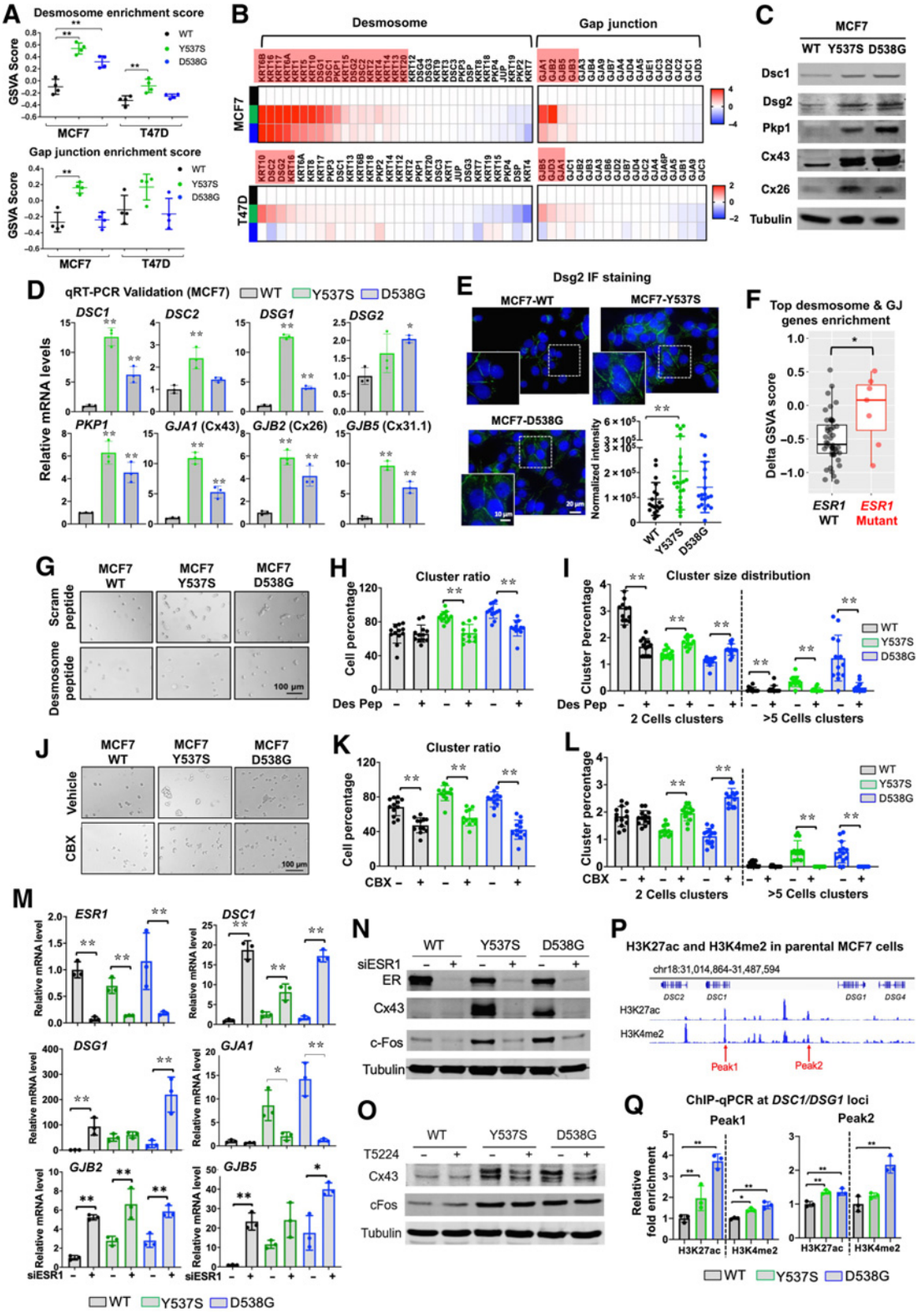

S12B), suggesting that epigenetic activation modulates gene expression in this particular context. We further evaluated active histone modifications on our target gene loci in the MCF7 model. We observed enhanced H3K27ac and H3K4me2 recruitment in both MCF7-Y537S and D538G cells at the nearest two histone modification sites around the *DSC1* and *DSG1* loci, the two most upregulated desmosome component genes in MCF7-mutant cells (**Fig. 3P**), suggesting activation of desmosome genes via an indirect ER-mediated epigenetic activation (**Fig. 3Q**).

ESR1 mutations promote reduced adhesive and enhanced invasive properties via altered *TIMP3*-MMP axis

In addition to altered cell–cell adhesion, metastasis is also mediated by coordinated changes in cell–matrix interaction (47, 48). Therefore, we assessed whether mutant ER affects interaction with the ECM. Computational analysis showed inverse correlation between ECM receptor pathway signatures and *ESR1* mutation status in the DFCI cohort with the same trend appearing in two of three of the remaining cohorts (**Fig. 4A**; Supplementary Fig. S13A; Supplementary Table S6). Employing an adhesion array on seven major ECM components, we observed that the MCF7 *ESR1*-mutant cell lines consistently lacked adhesive properties on almost all ECM components with the exception of fibronectin, and T47D *ESR1*-mutant cells displayed reduced adhesion on collagen I, collagen II, and fibronectin (**Fig. 4B**). Considering that collagen I is the most abundant ECM component in ER^+ breast cancer (Supplementary Fig. S13B), we repeated the adhesion assay on collagen I (**Fig. 4C** and **D**; Supplementary Fig. S13C and S13D) and similarly found reduced adhesion in both ER-mutant cells. In an orthogonal approach, we visualized and quantified adhesion in a coculture assay on collagen I using differentially labeled *ESR1* WT and mutant cells, which confirmed significantly decreased adhesive properties in the mutant cells (Supplementary Fig. S13E and S13F). Of note, *ESR1*-mutant adhesion deficiency on collagen I was also observed in two additional *ESR1*-mutant models (Supplementary Fig. S13G).

We sought to investigate the molecular mechanisms underlying the unique defect of collagen I adhesion in *ESR1*-mutant cells. There was no consistent change in expression of members of the integrin gene family, encoding well-characterized direct collagen I adhesion receptors, in our cell line models (Supplementary Fig. S14A; Supplementary Table S6). We therefore hypothesized that another gene critical in regulation of ECM genes might be altered and to test this directly, we performed gene expression analysis of 84 ECM adhesion-related genes using a qRT-PCR array (Supplementary Table S8). Pairwise comparisons between each mutant cell line and corresponding WT cells revealed a strong context-dependent pattern of ECM network reprogramming, with more pronounced effects in MCF7 cells (**Fig. 4E**). Intersection between Y537S and D538G mutants showed 23 and 1 consistently altered genes in MCF7 and T47D cells, respectively (**Fig. 4F**). *TIMP3*, the gene encoding tissue metallopeptidase inhibitor 3, was the only shared gene between all four mutant cell models (**Fig. 4F**), and we confirmed its decreased expression at the mRNA (**Fig. 4G**; Supplementary Fig. S14B) and protein level (**Fig. 4H**), as well as in other genome-edited *ESR1*-mutant models (Supplementary Fig. S14C). E2 treatment represses *TIMP3* expression, suggesting that

Figure 3.

Desmosome and gap junction adhesome reprogramming confers enhanced adhesive properties in *ESR1*-mutant cells. **A,** Gene Set Variation Analysis (GSVA) scores of desmosome and gap junction gene sets enrichment in MCF7 and T47D *ESR1* mutant versus WT cell RNA-seq datasets. Each cell type has four biological replicates. Dunnett test was used to test the significance between WT and mutant cell lines. **, $P < 0.01$. **B,** Heatmaps showing all desmosome and gap junction component genes in MCF7 and T47D *ESR1*-mutant cells. Data were extracted from RNA-seq results with four biological replicates. Color scale represents the $\log_2$ FCs in each mutant normalized to WT counterparts using the $\log_2$(TPM+1) expression matrix. Genes with counts = 0 in more than one replicate in each cell type were filtered out of analysis. Genes with a $\log_2$FC > 1.2 and a $P < 0.05$ in at least one group are labeled in red. **C,** Western blot validation of the expression level of *DSG2*, *DSC1*, *PKP1*, Cx43, and Cx26 in MCF7 WT and *ESR1*-mutant cells after hormone deprivation. Tubulin was blotted as a loading control. Representative blots from three independent repeats are shown for each protein. **D,** qRT-PCR validation of selected altered candidate desmosome and gap junction genes in MCF7 *ESR1*-mutant cells. $\Delta\Delta C_t$ method was used to analyze relative mRNA FCs normalized to WT cells, and *RPLP0* levels were measured as an internal control. Each bar represents mean ± SD with biological triplicates. This experiment is a representative of four independent repeats. Dunnett test was used to compare the gene expression between WT and each mutant. *, $P < 0.05$; **, $P < 0.01$. **E,** Representative images of immunofluorescence staining showing the distribution of desmoglein 2 (*DSG2*) in MCF7 WT and *ESR1*-mutant cells. Images were taken under ×20 magnification. A 2× zoom in of each image is presented. Bottom right, *DSG2* signal intensities were quantified and normalized to cell numbers in each image. Data from 20 regions within the collected images were combined from four independent experiments. Mean ± SD is presented in each plot. Dunnett test was used to test the significance between WT and mutant cells. **, $P < 0.01$. **F,** Box plots representing GSVA scores of the enrichment of the top desmosome and gap junction candidate genes (genes with $\log_2$FC > 2 in at least one mutant line) in patient-matched primary metastatic paired samples. Delta GSVA score of each sample was calculated by subtracting the scores of primary tumors from the matched metastatic tumors. Four quantiles are shown in each plot. Mann–Whitney *U* test was performed to compare the Delta GSVA scores between *ESR1* WT ($n = 44$) and mutation ($n = 7$) harboring tumors. *, $P < 0.05$. **G** and **J**, Representative images of cell cluster status after 2 hours of flow under physiologic shear stress in the ibidi microfluidic system, with or without 300 μmol/L of the desmosomal blocking peptide (**G**) or 100 μmol/L of carbenoxolone (**J**) treatment. Images were taken under ×10 magnification. This experiment is a representative from two (desmosome peptide treatment) and three (CBX treatment) independent repeats. **H** and **K**, Bar graphs representing the T0 normalized percentage of cells in cluster status after quantification of cluster and single-cell numbers under each treatment. Each bar represents mean ± SD quantified from 12 images per group. This experiment is a representative from two (desmosome peptide treatment) and three (CBX treatment) independent repeats. Student *t* test was used to examine the effects of treatment between each group's cluster ratio. **, $P < 0.01$. **I** and **L**, Bar graphs representing the T0 normalized two-cell and greater than five-cell cluster percentages under each treatment. Each bar represents mean ± SD quantified from 12 images per group. This experiment is a representative from two (desmosome peptide treatment) and three (CBX treatment) independent repeats. Pairwise Student *t* test was used to examine the effects of treatment between each group's cluster ratio. **, $P < 0.01$. **M,** Bar graphs representing qRT-PCR measurement of *DSC1*, *DSC2*, *GJA1*, *GJB2*, and *GJB5* mRNA levels in MCF7 WT and *ESR1*-mutant cells following siRNA knockdown of *ESR1* for 7 days. $\Delta\Delta C_t$ method was used to analyze relative mRNA FCs normalized to WT cells and *RPLP0* levels were measured as an internal control. Each bar represents mean ± SD with three biological replicates. Representative experiment from three independent repeats is displayed. Student *t* test was used to compare the gene expression between scramble and knockdown groups of each cell type. *, $P < 0.05$; **, $P < 0.01$. **N** and **O,** Western blot validation of the expression level of ER, Cx43, and cFOS in MCF7 WT and *ESR1*-mutant cells after 7 days of *ESR1* knockdown (**N**) or 3 days of 20 μmol/L T-5224 treatment (**O**). Tubulin was blotted as a loading control. Representative blot from three (**N**) and five (**O**) independent repeats is displayed. **P,** Screenshot of H3K27ac and H3K4me2 binding peaks at proximity to genomic *DSC1* and *DSG1* loci in MCF7 parental cells. ChIP-seq data were visualized at WashU Genome Browser based on public available dataset from ENCODE (H3K4me2, ENCSR875KOJ; H3K27ac, ENCSR752UOD). *Y*-axis represents the binding intensity of each ChIP-seq dataset. Selected peaks for ChIP-qPCR assessment in **Q** are indicated. **Q,** Bar graph showing the fold enrichment levels of the two active histone modification markers at the two selected peaks around *DSC1* and *DSG1* gene loci illustrated in **P**. Each bar represents mean ± SD from biological triplicates. Fold enrichment levels were calculated by normalizing to IgG controls and further normalized to WT levels. This experiment is representative of two independent repeats. Dunnett test was used within each group. ($N = 2$). *, $P < 0.05$; **, $P < 0.01$.

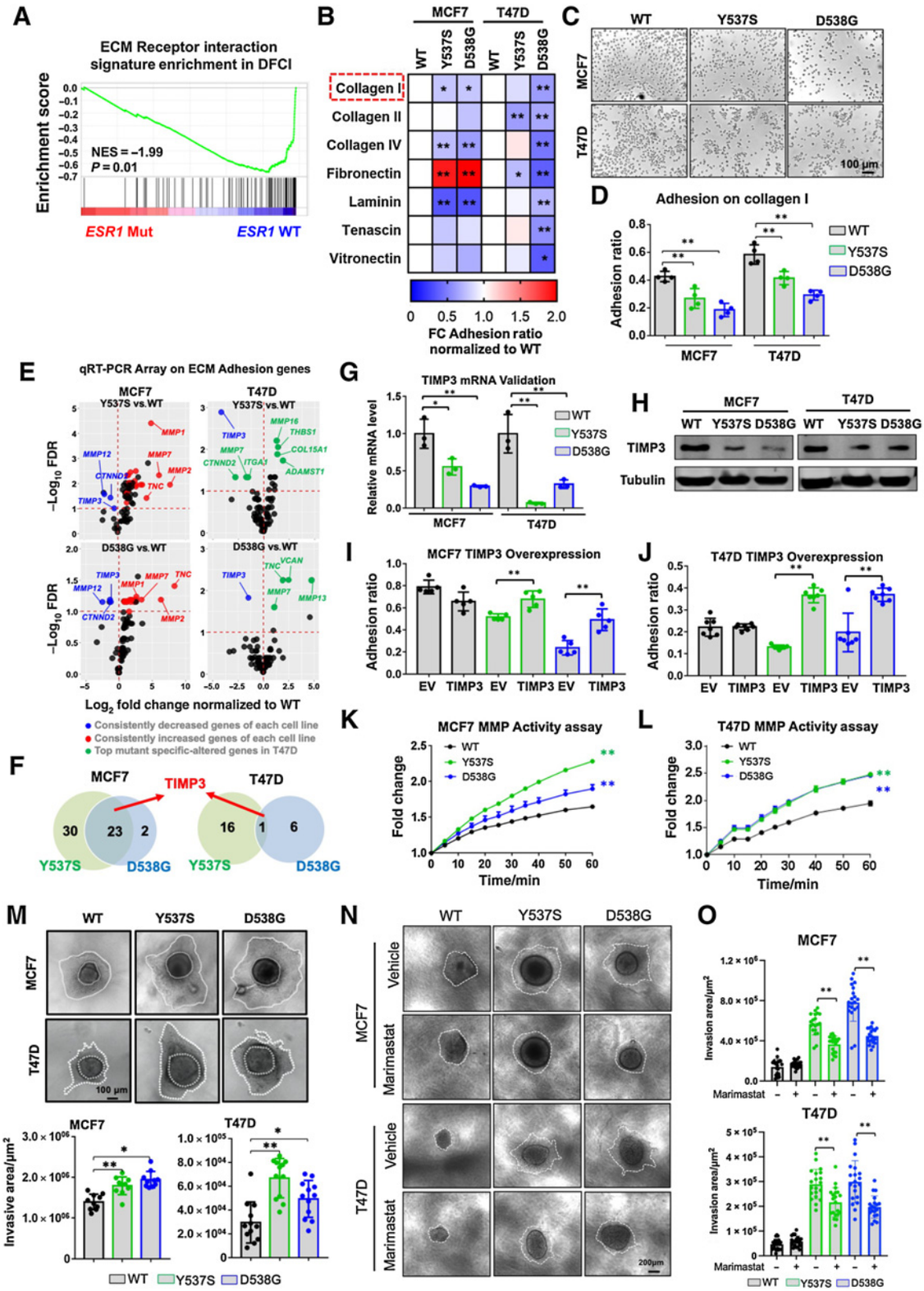

its downregulation in *ESR1*-mutant cells is likely due to ligand-independent repressive ER activity (Supplementary Fig. S14C). Downregulation of *TIMP3* was found in several (but not all) tamoxifen-resistant MCF7 models, but long-term estradiol deprived (LTED) MCF7 showed upregulation (Supplementary Fig. S14D). Furthermore, changes in *TIMP3* were not seen in other LTED models, suggesting that alteration of *TIMP3* by mutant *ESR1* is complex and warrants further investigation. Overexpression of *TIMP3* rescued the adhesion defect in *ESR1*-mutant cells (**Fig. 4I** and **J**; Supplementary Fig. S14E), with no impact on cell proliferation (Supplementary Fig. S14F). Collectively, these data imply a selective role for *TIMP3* downregulation in causing the decreased cell-matrix adhesion phenotype of the *ESR1*-mutant cells, consistent with a critical role for TIMP3 in metastasis in other cancer types (49, 50).

Given the role of *TIMP3* as an essential negative regulator of matrix metalloproteinase (MMP) activity, we compared MMP activity between *ESR1* WT and mutant cells. A pan-MMP enzymatic activity assay revealed significantly increased MMP activation in all mutant cells (**Fig. 4K** and **L**), indicating that the *ESR1*-mutant cells have increased capacity for matrix digestion. This was validated in spheroid-based invasion assays in which cells were embedded in collagen I (**Fig. 4M**) but without notable growth differences (Supplementary Fig. S15A and S15B). This was additionally visualized in coculture spheroid invasion assays using differentially labeled T47D *ESR1* WT and mutant cells, which showed an enrichment of *ESR1*-mutant cells at the leading edge of the spheroids (Supplementary Fig. S15C). Finally, we tested whether MMP blockade could repress *ESR1* mutant–modulated invasive and adhesive alterations. Marimastat treatment substantially reduced the invasive phenotype of *ESR1*-mutant cells without inhibiting growth (**Fig. 4N** and **O**; Supplementary Fig. S15D). Furthermore, the reduced adhesive property was rescued by Marimastat treatment in *ESR1*-mutant cells (Supplementary Fig. S15E). These data demonstrate that decreased *TIMP3* expression, resulting in increased MMP activation causes enhanced matrix digestion associated with decreased adhesion to ECM, ultimately conferring invasive properties to *ESR1*-mutant cells.

De novo FOXA1-mediated Wnt pathway activation enhances of the T47D-D538G cell migration

T47D D538G cells showed increased *in vivo* tumorigenesis despite showing less pronounced adhesive phenotypes compared with T47D Y537S and MCF7 Y537S/D538G cells. Reasoning mutation and context-dependent metastatic activities of the mutant ER protein and having identified "Cellular Movement" as another top hit in our initial pathway analysis of differentially expressed genes in *ESR1*-mutant tumors (**Fig. 1D**), we assessed potential differences in cellular migration between the different models. Wound scratch assays identified significantly increased cell motility in the T47D-D538G model (**Fig. 5A** and **B**), but not in T47D-Y537S–mutant (**Fig. 5B**) or MCF7-mutant cells (Supplementary Fig. S16A and S16B). This enhanced motility was shared between the three individual T47D-D538G clones again excluding potential clonal artifacts (Supplementary Fig. S16C and S16D). Furthermore, we observed a different morphology of T47D-D538G cells at the migratory leading edges (**Fig. 5C**) further confirmed by larger and stronger assembly of F-actin filaments at the edge of T47D-D538G cell clusters (Supplementary Fig. S16E–S16H). To mimic collective migration from a cluster of cells, we utilized a spheroid-based collective migration assay on type I collagen (**Fig. 5D**). The distance to the leading edges of T47D-D538G–mutant cells was significantly longer compared with WT spheroids (**Fig. 5E**). In orthogonal approaches, enhanced migratory capacities of T47D-D538G cells were observed in coculture assay using labeled T47D-WT and D538G cells (Supplementary Fig. S16I and S16J) and in Boyden

Figure 4.

ESR1-mutant cells show diminished ECM adhesion and enhanced invasion via an altered *TIMP3*-MMP axis. **A,** Gene set enrichment plots showing the comparison of enrichment levels of the "KEGG ECM Receptor Interaction" gene set (MSigDB, M7098) between WT and mutant tumors in DFCI cohort (98 *ESR1* WT and 32 mutant tumors). **B,** Heatmap representation of adhesion ratio on seven ECM components performed with MCF7 and T47D *ESR1* WT and mutant cells. Adhesion ratio of each condition with biological quadruplicates was quantified by dividing the number of remaining cells after washing to the original total cells plated. All data were further normalized to WT cells within each cell line. This experiment was performed once. Dunnett test was applied to each condition of each cell line. *, $P < 0.05$; **, $P < 0.01$. **C,** Representative images *ESR1* WT and mutant cells remaining on collagen I after three PBS washes. Images were taken using ×4 magnification. Experiment displayed is representative from three independent repeats. **D,** Quantification of adhesion ratios on collagen I in each cell type. Bar graphs represent the mean ± SD with four biological replicates in each group. Dunnett test was utilized within each cell line to compare WT and mutant adhesion ratios. Experiment displayed is representative from 12 (MCF7) and 11 (T47D) independent repeats. **, $P < 0.01$. **E**, Volcano plots showing the alterations of 84 ECM adhesion genes in all mutant cell types in a pairwise comparison with the WT counterparts. Genes were prefiltered with an average $C_t < 35$ in at least one group. An FDR < 0.1 was considered as a significantly altered gene in *ESR1*-mutant cells. Overlapping downregulated (blue) or upregulated (red) genes between the two mutants of each cell line are further highlighted, with gene name labels for the top targets. Top changed genes in each T47D-mutant cells are labeled in green. This experiment was performed once. **F,** Venn diagrams showing the consistently differentially expressed genes between the two mutant variants within each cell line. *TIMP3* is highlighted as the only overlapping gene in all four *ESR1*-mutant cell types. **G,** qRT-PCR validation of *TIMP3* expression in WT and *ESR1*-mutant cells. C_t values were normalized to *RPLP0* and further normalized to WT cells. Bar graphs represent the mean ± SD with biological triplicates in each group. Representative experiment from seven independent repeats is shown. Dunnett test was utilized within each cell line. *, $P < 0.05$; **, $P < 0.01$. **H,** Western blot validation of *TIMP3* from whole cell lysates after hormone deprivation. Tubulin was used as a loading control. Representative experiment from six independent repeats is shown. **I** and **J,** Quantification of adhesion ratios on collagen I in each mutant variant following transfection of pcDNA empty vector or *TIMP3* plasmids in MCF7 (**I**) and T47D (**J**) cell models. Bar graphs represent the mean ± SD from five (MCF7) and seven (T47D) biological replicates. Representative experiment from four independent repeats is shown. Student *t* test was used to compare the empty vector and *TIMP3*-overexpressing groups. **, $P < 0.01$. **K** and **L,** Graphical view of pan-MMP FRET kinetic assay. MMPs in MCF7 (**K**) and T47D (**L**) cell lysates were preactivated and mixed with MMP substrates. Fluorescence was measured in a time course manner and normalized to T0 baseline and further normalized to WT cell readouts. Each point represents the mean ± SD value from three biological replicates. Representative experiment from four independent repeats is shown. Pairwise two-way ANOVA between WT and each mutant cell type was performed. **, $P < 0.01$. **M,** Top, representative images of the spheroid-based collagen invasion assay in *ESR1* WT and mutant cell models. MCF7 and T47D spheroids were mixed in collagen I for 4 and 6 days, respectively. Brightfield images were taken accordingly with ×10 magnification. Bottom, quantification of invasive areas within images. Invasive areas were calculated by subtracting each original spheroid area from the corresponding endpoint total area. Each bar represents mean ± SD, with 10 biological replicates. Experiments displayed are representative of three independent repeats from each cell line. Dunnett test was used to compare the difference between WT and mutant cells. *, $P < 0.05$; **, $P < 0.01$. **N,** Representative images of the spheroid-based collagen invasion assay with 10 μmol/L of Marimastat treatment in MCF7 (top) and T47D (bottom) cell models for 4 and 6 days, respectively. Images were taken under ×10 magnification. Experiment was performed with 20 biological replicates for once. **O,** Quantification of corresponding invasive areas from **N**. Student *t* test was used to compare the effects of Marimastat treatment to vehicle control. **, $P < 0.01$.

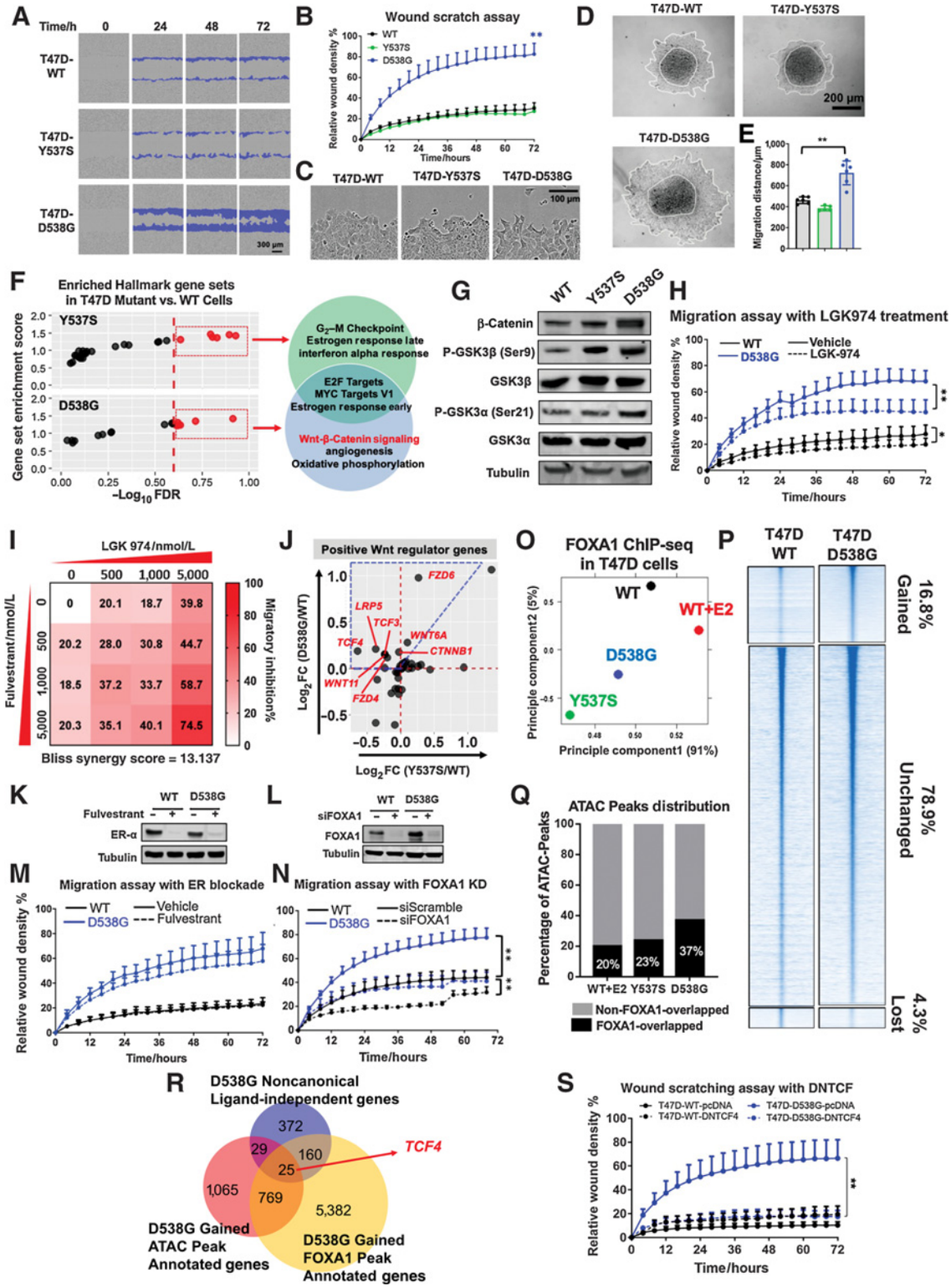

Figure 5.

De novo FOXA1-mediated Wnt pathway activation enhances migratory property of the T47D-D538G cells. **A** and **B,** Representative images (**A**) and quantification (**B**) of wound scratch assay of T47D WT and *ESR1*-mutant cells performed using IncuCyte live cell imaging system over 72 hours. The migratory region normalized to T0 are labeled in blue. Images were taken under ×10 magnification. Cell migration rates were quantified on the basis of relative wound densities, with eight biological replicates. Representative experiment from 11 independent repeats is shown. Pairwise two-way ANOVA between WT and each mutant was performed. **, $P < 0.01$. **C,** Representative magnified images of the migratory edge of each group in wound scratch assays in **A**. (*Continued on the following page.*)

chamber transwell assays (Supplementary Fig. S16K and S16L). Finally, in T47D overexpression models, we also observed significantly enhanced migration in D538G compared with WT-overexpressing cells (Supplementary Fig. S17A–S17E).

To understand the mechanisms underlying the migratory phenotype of T47D-D538G cells, we identified pathways uniquely enriched in these cells. Gene set enrichment analysis identified endocrine resistance-promoting pathways (e.g., E2F targets) in both T47D mutants, whereas Wnt/β-catenin signaling was one of the uniquely enriched pathways in T47D-D538G (**Fig. 5F**). Hyperactivation of the canonical Wnt/β-catenin pathway was further confirmed by a Top-Flash luciferase assay (Supplementary Fig. S18A). We also observed increased phosphorylation of GSK3β and GSK3α as well as β-catenin (both total and nuclear) protein levels in T47D-D538G cells (**Fig. 5G**; Supplementary Fig. S18B and S18C). Stimulation of T47D-WT cells with Wnt3A was not able to increase the migration to the same level of D538G cells (Supplementary Fig. S18D), suggesting that Wnt activation is a required but not sufficient factor in driving this phenotype. To address the potential clinical relevance of these findings, we utilized the porcupine inhibitor LGK974, which prevents the secretion of Wnt ligands and is currently being tested in a clinical trial for patients with advanced solid tumors including breast cancer (NCT01351103; refs. 51, 52). Treatment with LGK974 resulted in a 20% and 40% inhibition of T47D *ESR1* WT and D538G-mutant cell migration, respectively (**Fig. 5H**; Supplementary Fig. S18E) yet had no effect on cell proliferation (Supplementary Fig. S18F). We next studied the combination of LGK974 and the SERD, fulvestrant, in migration assays, in which we detected significant synergy (**Fig. 5I**), suggesting that combination therapy cotargeting the Wnt and ER signaling pathways might reduce the metastatic phenotypes of Wnt hyperactive *ESR1*-mutant tumors.

We sought to decipher the mechanisms underlying T47D-D538G Wnt hyperactivation. First, a set of Wnt component genes was identified to be uniquely enriched in tumors with D538G but not other mutant variants in the DFCI cohort (Supplementary Fig. S18G). Comparing the FCs of canonical Wnt signaling positive regulators between T47D-Y537S– and T47D-D538G–mutant cells, we identified eight candidate genes exhibiting pronounced enrichment in T47D-D538G cells (**Fig. 5J**), including ligands (e.g., *WNT6A*), receptors (e.g., *LRP5*), and transcriptional factors (e.g., *TCF4*). With the exception of *LRP5*, none of these candidate genes were induced by E2 stimulation in T47D *ESR1* WT cells (Supplementary Fig. S19A). Lack of consistent E2 regulation was confirmed in five additional ER^+ breast cancer cell lines (Supplementary Fig. S19B). Hence, we alternatively hypothesized that D538G ER might gain *de novo* binding sites proximal to Wnt pathway genes allowing their induction. We mapped ER binding globally by analyzing ER ChIP-seq in T47D WT and *ESR1*-mutant cells. Consistent with previous studies (11, 14), mutant ER were recruited to binding sites irrespective of hormone stimulation (Supplementary Fig. S19C; Supplementary Table S9). However, none of the mutant ER bound regions mapped to identified Wnt pathway genes (±50 kb of TSS), again suggesting a lack of direct canonical ER regulation. Moreover, short-term fulvestrant treatment only weakly dampened T47D-D538G cell migration (**Fig. 5K** and **M**), suggesting that ER activation may not be an essential prerequisite for enhanced cell migration in D538G cells.

Given our recent findings of enriched FOXA1 motifs in gained open chromatin of T47D-D538G cells (19), we decided to validate this pivotal *in silico* prediction, focusing on our observed migratory phenotype. In contrast to the limited effects of ER depletion, strikingly, FOXA1 knockdown fully rescued the enhanced migration in T47D-D538G cells (**Fig. 5L** and **N**), indicating a more dominant role of FOXA1 in controlling T47D-D538G cell migration. Ligand-independent two-dimensional growth of T47D-D538G cells was inhibited by both fulvestrant and FOXA1 knockdown

(*Continued.*) **D** and **E,** Representative images (**D**) and quantification (**E**) of spheroid collective migration assays in T47D-mutant cells. T47D cells were initially seeded into round bottom ULA plates to form spheroids, which were then transferred onto collagen I–coated plates. Collective migration was measured after 4 days. The migratory edge of each spheroid is circled with a white line. Migratory distances were calculated on the basis of the mean radius of each spheroid normalized to corresponding original areas. Representative experiment from three independent repeats is shown. Dunnett test was used for statistical analysis. **, $P < 0.01$. **F,** Dot plots representing the enrichment distribution of the 50 MSigDB curated Hallmark gene sets in T47D-Y537S and T47D-D538G models normalized to WT cells. Significantly enriched gene sets (FDR < 0.25) are highlighted in red, with names labeled in the Venn diagram plot on the right. Gene sets enriched in Y537S and D538G cell models are in green and blue circles, respectively. **G,** Immunoblot detection of β-catenin, phospho-GSK3β (Ser9), phospho-GSK3α (Ser21) total GSK3β, and total GSK3α levels in T47D WT and mutant cells after hormone deprivation. Tubulin was blotted as a loading control. Representative blots from three independent repeats are displayed for each protein. **H,** Quantification of IncuCyte wound scratch assay with or without 5 μmol/L LGK974 treatment for 72 hours. The migratory region normalized to T0 is labeled in blue. Images were taken under ×10 magnification. Cell migration rates were quantified on the basis of relative wound densities, with eight biological replicates. Representative experiment from three independent repeats is shown. Pairwise two-way ANOVA between WT and each mutant was performed. **, $P < 0.01$. **I,** IncuCyte migration assay with combination treatment of four different doses of LGK974 and fulvestrant in T47D-D538G cells. Inhibition rates were calculated using the wound density at 48 hours normalized to vehicle control, with values labeled using color scales in the heatmap. Positive Bliss scores were considered a synergistic combination. Representative experiment from three independent repeats is shown. **J,** Dot plot representing the FCs of all Wnt signaling component genes in both T47D *ESR1*-mutant cell models normalized to WT cells. The blue dotted frame highlights the unique T47D-D538G enriched genes as well as genes that are enriched in both mutants, but with a larger magnitude of enrichment in the T47D-D538G cells. **K** and **L,** Immunoblot validation of fulvestrant-induced ER degradation (**K**) and FOXA1 knockdown (**L**). Cell lysates were subjected to ER and FOXA1 detection. Tubulin was blotted as a loading control. These validation experiments were performed once. **M** and **N,** Wound scratch assay in T47D-D538G and WT cells with 1 μmol/L of fulvestrant treatment (**M**) or knockdown of FOXA1 (**N**) for 72 hours. Cell migration rates were quantified on the basis of wound closure density. For fulvestrant treatment, data were merged from three (WT) or six (D538G) independent experiments. For FOXA1 knockdown, representative result from three independent repeats is displayed. Pairwise two-way ANOVA between siScramble/siFOXA1 or vehicle/fulvestrant conditions in each cell type was performed. **, $P < 0.01$. **O,** PCA plot showing the FOXA1 peak distribution of T47D WT, WT+E2, T47D-Y537S, and T47D-D538G groups. **P,** Heatmaps representing the comparison of FOXA1 binding intensities in T47D-D538G mutants with FOXA1 binding in WT cells. Displayed in a horizontal window of ± 2 kb from the peak center. The pairwise comparison between WT and mutant samples was performed to calculate the FC of intensities. Binding sites were subclassified into sites with increased intensity (FC > 2), decreased intensity (FC <− 2), and nonchanged intensity (−2 < FC < 2). Percentages of each subgroup are labeled on the heatmaps. **Q,** Bar charts showing the percentage of ATAC peaks overlapping (black) or not overlapping (gray) with FOXA1 binding sites in T47D-WT, T47D-Y537S, and T47D-D538G cells. **R,** Venn diagram showing the intersection of genes annotated from dually gained ATAC and FOXA1 peaks (±3 kb of TSS with 200 kb of the peak flank) and RNA-seq differentially expressed noncanonical ligand-independent genes (gene with |FC| > 2, FDR < 0.005 in D538G vs. WT excluding genes with |FC| > 1.5, FDR < 0.01 in WT + E2 vs. WT groups). *TCF4* is highlighted. **S,** Wound scratch assay in T47D-WT and T47D-D538G cells with or without prior transfection of a dominant negative *TCF4* plasmid for 72 hours. Pairwise two-way ANOVA between vehicle and treatment conditions was performed. Data from one representative experiment of three independent experiments (each with six biological repeats) are shown. **, $P < 0.01$.

(Supplementary Fig. S19D), suggesting a canonical ER-FOXA1 coregulatory mechanism in growth, distinguished from the role of FOXA1 in the regulation of migration.

To further explore how FOXA1 contributes to the migratory phenotype, we performed FOXA1 ChIP-seq to decipher the genomic binding profiles. We identified approximately 30,000 peaks in T47D WT cells regardless of E2 stimulation and a approximately 1.6-fold increase in binding sites of the Y537S (61, 934) and D538G (54, 766) ER mutants (Supplementary Fig. S20A; Supplementary Table S9). PCA distinctly segregated all four groups (**Fig. 5O**), suggesting unique FOXA1 binding site redistribution. Comparison of binding intensities revealed 14%, 28%, and 21% FOXA1 binding sites were altered in WT+E2, Y537S and D538G groups, respectively, with a predominant gain of binding intensities in the two T47D mutants (**Fig. 5P**; Supplementary Fig. S20B).

Because FOXA1 is a well-known essential pioneer factor of ER in breast cancer, we examined interplay between FOXA1 and WT and mutant ER. Interestingly, both Y537S (39%) and D538G (25%) ER binding sites showed a significantly lower overlap between FOXA1 compared with the WT+E2 group (56%), albeit with the increased number of gained mutant FOXA1 binding sites (Supplementary Fig. S20C). This discrepancy suggests that FOXA1 exhibits a diminished ER pioneering function and instead might contribute to novel functions via gained *de novo* binding sites. Co-occupancy analysis using isogenic ATAC-seq data (19) uncovered that the open chromatin of T47D-D538G cells was more associated with FOXA1 binding sites compared with WT and T47D-Y537S cells (**Fig. 5Q**). FOXA1 binding intensities were also stronger in D538G ATAC sites (Supplementary Fig. S20D). Collectively, these results provide evidence that FOXA1 likely plays a critical role in the D538G-mutant cell to reshape its accessible genomic landscape.

We further investigated the impact of the gained FOXA1-associated open chromatin on transcriptomes, particularly exploring *ESR1* mutant–specific genes. Intersection of the gained FOXA1 and ATAC sites for annotated T47D-D538G genes with noncanonical ligand independence identified 25 potential targets that could be attributed to *de novo* FOXA1 bound open chromatin, exemplified by *PRKG1* and *GRFA* as top targets (**Fig. 5R**; Supplementary Fig. S21A). Notably, one of our identified D538G specific Wnt regulator genes, *TCF4*, was uncovered in this analysis. Higher *TCF4* expression in T47D-D538G cells was validated by qRT-PCR and furthermore this increased expression could be fully blocked following FOXA1 knockdown (Supplementary Fig. S21B). In addition, stronger FOXA1 recruitment at the *TCF4* gene locus was validated via ChIP-qPCR (Supplementary Fig. S21C and S21D). Importantly, overexpression of dominant negative *TCF4* strongly impaired cell migration in T47D-D538G, while it only slightly affected WT cells (**Fig. 5S**). Together, these results support that FOXA1 binding site redistribution leads to novel chromatin remodeling and enhanced expression of genes with roles in metastases including *TCF4*, which subsequently activate Wnt-driven migration in T47D-D538G cells.

Discussion

Hotspot somatic mutations clustered in the LBD of ER represent a prevalent molecular mechanism that drives antiestrogen resistance in approximately 30% of advanced ER^+ breast cancer. There is an urgent need for a deeper understanding of this resistance mechanism to develop novel and personalized therapeutics. Utilizing clinical samples, *in silico* analysis of large datasets, and robust and reproducible experimentation in multiple genome-edited cell line models, our study uncovers complex and context-dependent mechanisms of how *ESR1* mutations confer gain-of-function metastatic properties. We identified *ESR1* mutations as multimodal metastatic modulators hijacking adhesive and migratory networks, and thus likely influencing metastatic pathogenesis and progression. Mechanistically, we uncovered novel ER-indirect regulation of metastatic candidate gene expression, distinct from previously described (11, 12, 53) canonical ligand-independent gene induction. Nonetheless, some limitations were noted in our study, such as the lack of *in vivo* validation of studied therapeutic approaches and lack of proposed target validation in clinical specimens. In addition, our numbers for clinical samples of paired primary-metastatic tumors harboring *ESR1* mutations is finite, necessitating validation in future studies with larger clinical cohorts.

We discovered enhanced cell–cell adhesion via upregulated desmosome and gap junction networks in cell lines and clinical samples with *ESR1* mutations. These transcriptional alterations are associated with a specific clinical phenotype characterized not only by treatment resistance, but also by high CTC count and a different metastatic organotropism (54, 55). We propose that this key alteration may support increased metastases in ER-mutant tumors through facilitating the formation of homotypic or heterotypic CTC clusters, providing a favorable environment for CTC dissemination, as described previously (33). This idea is further supported by previous data showing upregulation of the desmosome gene plakoglobin (*JUP*), which may play a role in a CTC cluster formation signature (33). We observed increased expression of plakophilin, desmocollin, and desmoglein in *ESR1*-mutant cells, suggesting the importance of the broad desmosome network reprogramming for functional cell clustering activity. Moreover, enhanced gap junction genes might potentiate intercellular calcium signaling, facilitating the prolonged survival of various metastatic cell types tethered to *ESR1*-mutant cells *en route* (56). Dissociation of CTC cluster using Na+/K+ ATPase inhibitors decreased metastasis *in vivo* (40). In addition, previous studies have validated the antitumor effects of FDA-approved gap junction blockers carbenoxolone *in vivo* (57). Our results warrant additional preclinical studies using drugs targeting desmosome and gap junctions, with the ultimate goal of applying these treatments in a CTC-targeted clinical trial to improve outcomes for patients harboring breast cancers with *ESR1* mutations.

Previous studies using similar *ESR1*-mutant cell models described enhanced migratory properties (15, 16), but no mechanistic explanations were uncovered. Here we identify a critical role for Wnt/β-catenin signaling and show that cotargeting of Wnt and ER resulted in synergistic inhibition of cell migration. Intriguingly, the strong effect we observed on migration was unique to T47D-D538G cells, a discovery that was made possible through our use of multiple genome-edited mutation models. This finding might help explain the higher frequency of D538G mutations in metastatic samples, despite the stronger endocrine resistance phenotype of Y537S mutation (5, 12, 14, 32). Markedly, although we highlighted the upregulation of *TCF4* as an outcome of *de novo* FOXA1 reprogramming, it is plausible that other increased Wnt regulators including receptors (e.g., LRP5) and ligands (e.g., WNT6A) are also associated with the migratory phenotypes. Hence LGK974, a Wnt secretion inhibitor, could efficiently abrogate this phenotype. Of note, slightly higher Wnt activity and β-catenin accumulation were also observed in T47D-Y537S cells, but this failed to convert into a migratory phenotype. It is possible that some genes uniquely regulated by Y537S ER in T47D cells might inhibit migratory phenotypes. For instance, the gap junction component, connexin 43, which is exclusively upregulated in T47D-Y537S cells, has been reported to play an inhibitory role in epithelial

cell migration (58). Furthermore, the unique observation in T47D rather than MCF7 cell line may be in part explained by the lower basal migratory property and basal Wnt activation in the T47D cell line, which might allow additional gain of function. MCF7 WT cells showed approximately 4-fold higher wound closure ratio than T47D at 72 hours (**Fig. 5B**; Supplementary Fig. S16A) and furthermore it expresses truncated mutant version of LRP5 (59), which confers constitutive Wnt signaling activation. *In vivo* experiments revealed enhanced metastasis in the MCF7-Y537S but not D538G model. This discrepancy with the *in vitro* data could possibly be explained by the longer distant metastatic latency requirement of D538G cells *in vivo*, consistent with a recent study using overexpression cell models (14). Alternatively, it is also plausible that Y537S-mutant cells exhibit stronger *in vivo* outgrowth at metastatic sites. Further *in vivo* metastatic experiments in the absence and presence of E2 are warranted to delineate the reason. These data support strong allele and context-dependent effects of the *ESR1* mutation on metastatic phenotypes, in line with context-dependent effects on transcriptome, cistromes, and accessible genome in *ESR1*-mutant cells (11, 12, 14, 19). Of note, previous efforts using multiple cell line models with *ESR1* mutations elucidated several congruent molecular and functional alterations associated with endocrine resistance (14, 15, 53), suggesting that mechanisms underlying metastasis of *ESR1*-mutant clones exhibit a higher degree of heterogeneity. This is also supported by clinical data: the recent BOLERO2 trial showed significant differences in OS and everolimus response between Y537S and D538G mutations (9), and results from the recent PALOMA3 trial suggest a potential palbociclib resistance uniquely gained in tumors bearing the Y537S mutation (60). Given our model are limited to MCF7 and T47D cells, there's a pressing need to establish additional *ESR1*-mutant models with different background to follow-up on our observation and to perform further preclinical investigations. Taken together, these proof-of-concept studies are setting the stage for a more contextual and personalized therapeutic targeting strategy in *ESR1*-mutant breast cancer.

Of note, our comprehensive clinical investigation from five different cohorts ($N = 996$) suggest that *ESR1* mutations more common in distant compared with local recurrences, which we propose is due to gain-of-function of *ESR1*-mutant clones that is those cells are more equipped to escape from the local-regional microenvironment. However, there are some limitations to our study. First, it is challenging to differentiate local recurrences from secondary primary tumors, limiting our analysis. Second, in some of the cohorts, we observed significant differences in number of lines of therapy and time to recurrence comparing patients (i) with *ESR1* WT versus mutant tumors, and (ii) with local and distance recurrences. Although these analyses are limited by different numbers of cases, and data that are available, nevertheless, they suggest that lack of *ESR1* mutation in local recurrences could at least in part be also due to differences in prior therapies as reported previously (6). Of note, a recent study identified hotspot *ESR1* mutations in 15 of 41 (36%) of local-regional ER^+ recurrences albeit at significantly lower mutation allele frequencies (61). Given our data presented in this study, together with prior data (14–16), we propose that *ESR1* mutations can facilitate metastatic spread although they might not be sufficient to function as genetic drivers for such events.

Finally, we also sought to address the ER regulatory mechanisms involved in induction of candidate metastatic driver genes utilizing ChIP-seq technology. Interestingly, none of the metastatic candidate genes in *ESR1*-mutant cells gained proximal ER binding sites. This could be a result of our stringent hormone deprivation protocol resulting in depletion of weaker binding events, and thus less sensitive binding site readouts. This idea is supported by ChIP-seq data from Harrod and colleagues (11), which shows stronger ER binding sites around *DSC2*, *DSG2*, and *TIMP3* gene loci in MCF7-Y537S cells. Our data, however, clearly show that ER-mutant cells display changes in indirect gene regulation, resulting in metastatic phenotypes. This observation is due to noncanonical ER action on chromatin structure remodeling, which was alternatively validated from our ATAC-seq and FOXA1 ChIP-seq data. We propose that mutant ER reprograms FOXA1, resulting in redistribution of FOXA1 binding to specific enhancers controlling the key migratory driver gene(s). It is also likely that mutant ER can impact FOXA1 occupancy by cooperating with other known epigenetic regulators such as GATA3 (62). In addition, *ESR1* mutations might alter the expression of several important histone modifiers such as KDM5B and KMT2C, which showed expression changes in *ESR1*-mutant cells. Alteration of histone writers or erasers may reshape global H3K4 methylation and thus differentially recruit FOXA1 (63). These mechanisms warrant future investigation. In addition, several recent studies uncovered the promising role of androgen receptor (AR) in *ESR1*-mutant tumors and cell models (18, 64), and additional studies are warranted to study *de novo* interplay between FOXA1, AR, and mutant ER.

Overall, our study serves as a timely and important preclinical report uncovering mechanistic insights into *ESR1* mutations that can pave the way toward personalized treatment of patients with advanced MBC.

Authors' Disclosures

M.E. Yates reports grants from NIH during the conduct of the study. K.M. Levine reports grants from NIH during the conduct of the study. S. Ali reports grants from Cancer Research UK, Breast Cancer Now, and Medical Research Council UK during the conduct of the study; grants, personal fees, and other support from Carrick Therapeutics Ltd. and non-financial support and other support from AstraZeneca outside the submitted work. L. Buluwela reports grants from Cancer Research UK, Breast Cancer Now, and Medical Research Council UK during the conduct of the study; grants from Carrick Therapeutics Ltd. and non-financial support and other support from AstraZeneca outside the submitted work. J. Gertz reports grants from Department of Defense during the conduct of the study. L. Gerratana reports personal fees from Eli Lilly and Novartis during the conduct of the study. M. Cristofanilli reports grants and personal fees from Lilly, Menarini, Pfizer; personal fees from Foundation Medicine, Guardant Health, Olaris, and Cytodyn outside the submitted work. P. Sundd reports grants from Novartis AG, CSL Behring Inc, IHP Therapeutics, and Bayer Inc. outside the submitted work. E. Guerini-Rocco reports grants and non-financial support from Thermo Fisher Scientific; personal fees and non-financial support from Novartis, Roche; personal fees from Exact Sciences; and grants, personal fees, and non-financial support from AstraZeneca outside the submitted work. N. Wagle reports personal fees from Eli Lilly and Co., Relay Therapeutics, Flare Therapeutics, and grants from Puma Biotechnologies outside the submitted work. P. Jank reports other support from Myriad Genetics, Inc. outside the submitted work. C. Denkert reports personal fees from Roche, MSD Oncology, Daiichi Sankyo, AstraZeneca, Molecular Health, Lilly; grants from Myriad; and other support from Sividon outside the submitted work. M.M. Karsten reports personal fees from AstraZeneca and Roche outside the submitted work. B.H. Park is a paid consultant for Jackson Labs, EQRx, Sermonix, Hologics, Guardant Health and is a paid scientific advisory board member for Celcuity Inc. B.H. Park also has research contracts with GE Healthcare, Lilly, and Pfizer. Under separate licensing agreements between Horizon Discovery, LTD. and The Johns Hopkins University, B.H. Park is entitled to a share of royalties received by the University on sales of products. The terms of this arrangement are being managed by the Johns Hopkins University in accordance with its conflict of interest policies. P.C. Lucas reports other support from NSABP Foundation and grants from NIH outside the submitted work; in addition, P.C. Lucas has a patent for Small Molecules and Their Use as MALT1 Inhibitors pending; and has received compensation from Schrodinger Inc. (speaker fee; spouse) and holds stock in Amgen, both outside the scope of submitted work. S. Oesterreich is married to Dr. Adrian Lee, co-author of the study. S. Oesterreich has obtained funding for the submitted work as indicated in the article; however, none of them represents a conflict of interest. No disclosures were reported by the other authors.

Authors' Contributions

Z. Li: Conceptualization, resources, data curation, software, formal analysis, investigation, visualization, methodology, writing–original draft, project administration, writing–review and editing. **Y. Wu:** Data curation, formal analysis, validation, visualization, writing–review and editing. **M.E. Yates:** Validation, writing–review and editing. **N. Tasdemir:** Data curation, formal analysis, writing–review and editing. **A. Bahreini:** Data curation, formal analysis, writing–review and editing. **J. Chen:** Validation. **K.M. Levine:** Formal analysis, validation, writing–review and editing. **N.M. Priedigkeit:** Resources, writing–review and editing. **A. Nasrazadani:** Data curation. **S. Ali:** Resources, writing–review and editing. **L. Buluwela:** Resources, writing–review and editing. **S. Arnesen:** Resources, writing–review and editing. **J. Gertz:** Resources, writing–review and editing. **J.K. Richer:** Resources, writing–review and editing. **B. Troness:** Data curation, methodology. **D. El-Ashry:** Conceptualization, data curation, formal analysis, supervision, writing–review and editing. **Q. Zhang:** Resources. **L. Gerratana:** Resources, methodology, writing–review and editing. **Y. Zhang:** Resources, methodology. **M. Cristofanilli:** Conceptualization, resources, supervision, methodology, writing–review and editing. **M.A. Montanez:** Methodology. **P. Sundd:** Methodology. **C.T. Wallace:** Methodology. **S.C. Watkins:** Conceptualization, supervision, methodology. **C. Fumagalli:** Resources, data curation. **E. Guerini-Rocco:** Resources, data curation. **L. Zhu:** Formal analysis, validation, writing–review and editing. **G.C. Tseng:** Software, supervision, writing–review and editing. **N. Wagle:** Resources. **J.S. Carroll:** Conceptualization, writing–review and editing. **P. Jank:** Resources. **C. Denkert:** Resources, writing–review and editing. **M.M. Karsten:** Resources, writing–review and editing. **J.-U. Blohmer:** Resources. **B.H. Park:** Resources, writing–review and editing. **P.C. Lucas:** Methodology, writing–review and editing. **J.M. Atkinson:** Formal analysis, supervision, validation, investigation, project administration, writing–review and editing. **A.V. Lee:** Conceptualization, formal analysis, supervision, funding acquisition, investigation, writing–original draft, project administration. **S. Oesterreich:** Conceptualization, resources, supervision, funding acquisition, investigation, writing–original draft, project administration.

Acknowledgments

This work was supported by the Breast Cancer Research Foundation (A.V. Lee, B.H. Park, and S. Oesterreich); Susan G. Komen Scholar awards (SAC110021 to A.V. Lee; SAC170078 to B.H. Park; SAC160073 to S. Oesterreich); the Metastatic Breast Cancer Network Foundation (S. Oesterreich); the NCI (R01CA221303 to S. Oesterreich; F30CA203154 to K.M. Levine; F30CA250167 to M.E. Yates); Department of Defense Breast Cancer Research Program (W81XWH1910434 to J. Gertz and W81XWH1910499 to S. Oesterreich), and the Fashion Footwear Association of New York, Magee-Womens Research Institute and Foundation, The Canney Foundation, The M&E Foundation, Nicole Meloche Foundation, Penguins Alumni Foundation, the Pennsylvania Breast Cancer Coalition, and the Shear Family Foundation. S. Oesterreich and A.V. Lee are Hillman Fellows. Z. Li is supported by John S. Lazo Cancer Pharmacology Fellowship. N. Tasdemir was supported by a Department of Defense Breakthrough Fellowship Award (BC160764) and an NIH Pathway to Independence Award (K99CA237736). This project used the UPMC Hillman Cancer Center Tissue and Research Pathology Services supported in part by NIH grant award P30CA047904.

The authors are grateful for advice, discussions, and technical support from Dr. Ye Qin, Dr. Yu Jiang, Dr. Min Yu, Yonatan Amzaleg, and Meghan S. Mooring. The authors would like to thank Dr. Peilu Wang for her contribution to earlier studies in the Lee-Oesterreich group on *ESR1* mutations. This project used the University of Pittsburgh HSCRF Genomics Research Core, the University of Pittsburgh Center for Research Computing, and the UPMC Hillman Cancer Center Tissue and Research Pathology Services supported in part by NIH grant award P30CA047904. The authors would like to thank the patients who contributed samples to the tissue bank as well as all the clinicians and staff for their efforts in collecting tissues.

The costs of publication of this article were defrayed in part by the payment of page charges. This article must therefore be hereby marked *advertisement* in accordance with 18 U.S.C. Section 1734 solely to indicate this fact.

Received August 3, 2021; revised November 3, 2021; accepted January 18, 2022; published first January 25, 2022.

References

1. DeSantis CE, Ma J, Goding Sauer A, Newman LA, Jemal A. Breast cancer statistics, 2017, racial disparity in mortality by state. CA Cancer J Clin 2017;67:439–48.
2. Turner NC, Neven P, Loibl S, Andre F. Advances in the treatment of advanced oestrogen-receptor-positive breast cancer. Lancet 2017;389:2403–14.
3. Spoerke JM, Gendreau S, Walter K, Qiu J, Wilson TR, Savage H, et al. Heterogeneity and clinical significance of ESR1 mutations in ER-positive metastatic breast cancer patients receiving fulvestrant. Nat Commun 2016;7:11579.
4. Robinson DR, Wu Y-M, Vats P, Su F, Lonigro RJ, Cao X, et al. Activating ESR1 mutations in hormone-resistant metastatic breast cancer. Nat Genet 2013;45:1446–51.
5. Toy W, Weir H, Razavi P, Lawson M, Goeppert AU, Mazzola AM, et al. Activating ESR1 mutations differentially affect the efficacy of ER antagonists. Cancer Discov 2017;7:277–87.
6. Schiavon G, Hrebien S, Garcia-Murillas I, Cutts RJ, Pearson A, Tarazona N, et al. Analysis of ESR1 mutation in circulating tumor DNA demonstrates evolution during therapy for metastatic breast cancer. Sci Transl Med 2015;7:313ra182–.
7. Wang P, Bahreini A, Gyanchandani R, Lucas PC, Hartmaier RJ, Watters RJ, et al. Sensitive detection of mono-and polyclonal ESR1 mutations in primary tumors, metastatic lesions, and cell-free DNA of breast cancer patients. Clin Cancer Res 2016;22:1130–7.
8. Zhang K, Hong R, Xu F, Xia W, Kaping L, Qin G, et al. Clinical value of circulating ESR1 mutations for patients with metastatic breast cancer: a meta-analysis. Cancer Manag Res 2018;10:2573–80.
9. Chandarlapaty S, Chen D, He W, Sung P, Samoila A, You D, et al. Prevalence of ESR1 mutations in cell-free DNA and outcomes in metastatic breast cancer: a secondary analysis of the BOLERO-2 clinical trial. JAMA Oncol 2016;2:1310–5.
10. Toy W, Shen Y, Won H, Green B, Sakr RA, Will M, et al. ESR1 ligand-binding domain mutations in hormone-resistant breast cancer. Nat Genet 2013;45:1439–45.
11. Harrod A, Fulton J, Nguyen VT, Periyasamy M, Ramos-Garcia L, Lai C-F, et al. Genomic modelling of the ESR1 Y537S mutation for evaluating function and new therapeutic approaches for metastatic breast cancer. Oncogene 2017;36:2286–96.
12. Bahreini A, Li Z, Wang P, Levine KM, Tasdemir N, Cao L, et al. Mutation site and context dependent effects of ESR1 mutation in genome-edited breast cancer cell models. Breast Cancer Res 2017;19:60.
13. Fanning SW, Mayne CG, Dharmarajan V, Carlson KE, Martin TA, Novick SJ, et al. Estrogen receptor alpha somatic mutations Y537S and D538G confer breast cancer endocrine resistance by stabilizing the activating function-2 binding conformation. Elife 2016;5:e12792.
14. Jeselsohn R, Bergholz JS, Pun M, Cornwell M, Liu W, Nardone A, et al. Allele-specific chromatin recruitment and therapeutic vulnerabilities of ESR1 activating mutations. Cancer Cell 2018;33:173–86.
15. Yu L, Wang L, Mao C, Duraki D, Kim JE, Huang R, et al. Estrogen-independent myc overexpression confers endocrine therapy resistance on breast cancer cells expressing ERαY537S and ERαD538G mutations. Cancer Lett 2019;442:373–82.
16. Merenbakh-Lamin K, Ben-Baruch N, Yeheskel A, Dvir A, Soussan-Gutman L, Jeselsohn R, et al. D538G mutation in estrogen receptor-α: a novel mechanism for acquired endocrine resistance in breast cancer. Cancer Res 2013;73:6856–64.
17. Gelsomino L, Gu G, Rechoum Y, Beyer AR, Pejerrey SM, Tsimelzon A, et al. ESR1 mutations affect anti-proliferative responses to tamoxifen through enhanced cross-talk with IGF signaling. Breast Cancer Res Treat 2016;157:253–65.
18. Gu G, Tian L, Herzog SK, Rechoum Y, Gelsomino L, Gao M, et al. Hormonal modulation of ESR1 mutant metastasis. Oncogene 2021;40:997–1011.
19. Arnesen S, Blanchard Z, Williams MM, Berrett KC, Li Z, Oesterreich S, et al. Estrogen receptor alpha mutations in breast cancer cells cause gene expression changes through constant activity and secondary effects. Cancer Res 2020;81:539–51.
20. Tselepis C, Chidgey M, North A, Garrod D. Desmosomal adhesion inhibits invasive behavior. Proc Natl Acad Sci U S A 1998;95:8064–9.
21. Runswick SK, O'Hare MJ, Jones L, Streuli CH, Garrod DR. Desmosomal adhesion regulates epithelial morphogenesis and cell positioning. Nat Cell Biol 2001;3:823–30.
22. Sikora MJ, Cooper KL, Bahreini A, Luthra S, Wang G, Chandran UR, et al. Invasive lobular carcinoma cell lines are characterized by unique estrogen-mediated gene expression patterns and altered tamoxifen response. Cancer Res 2014;74:1463–74.

23. Ianevski A, He L, Aittokallio T, Tang J. SynergyFinder: a web application for analyzing drug combination dose–response matrix data. Bioinformatics 2017;33:2413–5.
24. Razavi P, Chang MT, Xu G, Bandlamudi C, Ross DS, Vasan N, et al. The genomic landscape of endocrine-resistant advanced breast cancers. Cancer Cell 2018;34:427–38.
25. Paul MR, Pan T-c, Pant DK, Shih NN, Chen Y, Harvey KL, et al. Genomic landscape of metastatic breast cancer identifies preferentially dysregulated pathways and targets. J Clin Invest 2020;130:4252–65.
26. Pleasance E, Titmuss E, Williamson L, Kwan H, Culibrk L, Zhao EY, et al. Pan-cancer analysis of advanced patient tumors reveals interactions between therapy and genomic landscapes. Nat Cancer 2020;1:452–68.
27. Fumagalli C, Ranghiero A, Gandini S, Corso F, Taormina S, De Camilli E, et al. Inter-tumor genomic heterogeneity of breast cancers: comprehensive genomic profile of primary early breast cancers and relapses. Breast Cancer Res 2020;22:107.
28. Priedigkeit N, Hartmaier RJ, Chen Y, Vareslija D, Basudan A, Watters RJ, et al. Intrinsic subtype switching and acquired ERBB2/HER2 amplifications and mutations in breast cancer brain metastases. JAMA Oncol 2017;3:666–71.
29. Priedigkeit N, Watters RJ, Lucas PC, Basudan A, Bhargava R, Horne W, et al. Exome-capture RNA sequencing of decade-old breast cancers and matched decalcified bone metastases. JCI insight 2017;2:e95703.
30. Levine KM, Priedigkeit N, Basudan A, Tasdemir N, Sikora MJ, Sokol ES, et al. FGFR4 overexpression and hotspot mutations in metastatic ER+ breast cancer are enriched in the lobular subtype. NPJ Breast Cancer 2019;5:19.
31. Robinson DR, Wu Y-M, Lonigro RJ, Vats P, Cobain E, Everett J, et al. Integrative clinical genomics of metastatic cancer. Nature 2017;548:297–303.
32. Jia S, Miedel MT, Ngo M, Hessenius R, Chen N, Wang P, et al. Clinically observed estrogen receptor alpha mutations within the ligand-binding domain confer distinguishable phenotypes. Oncology 2018;94:176–89.
33. Aceto N, Bardia A, Miyamoto DT, Donaldson MC, Wittner BS, Spencer JA, et al. Circulating tumor cell clusters are oligoclonal precursors of breast cancer metastasis. Cell 2014;158:1110–22.
34. Ungefroren H, Sebens S, Seidl D, Lehnert H, Hass R. Interaction of tumor cells with the microenvironment. Cell Commun Signal 2011;9:18.
35. Friedl P, Locker J, Sahai E, Segall JE. Classifying collective cancer cell invasion. Nat Cell Biol 2012;14:777–83.
36. Jimenez MA, Tutuncuoglu E, Barge S, Novelli EM, Sundd P. Quantitative microfluidic fluorescence microscopy to study vaso-occlusion in sickle cell disease. Haematologica 2015;100:e390–3.
37. Ao Z, Shah SH, Machlin LM, Parajuli R, Miller PC, Rawal S, et al. Identification of cancer-associated fibroblasts in circulating blood from patients with metastatic breast cancer. Cancer Res 2015;75:4681–7.
38. Tasdemir N, Bossart EA, Li Z, Zhu L, Sikora MJ, Levine KM, et al. Comprehensive phenotypic characterization of human invasive lobular carcinoma cell lines in 2D and 3D cultures. Cancer Res 2018;78:6209–22.
39. Cunha S, Lin Y-C, Goossen EA, DeVette CI, Albertella MR, Thomson S, et al. The RON receptor tyrosine kinase promotes metastasis by triggering MBD4-dependent DNA methylation reprogramming. Cell Rep 2014;6:141–54.
40. Gkountela S, Castro-Giner F, Szczerba BM, Vetter M, Landin J, Scherrer R, et al. Circulating tumor cell clustering shapes DNA methylation to enable metastasis seeding. Cell 2019;176:98–112.
41. Cristofanilli M, Pierga J-Y, Reuben J, Rademaker A, Davis AA, Peeters DJ, et al. The clinical use of circulating tumor cells (CTCs) enumeration for staging of metastatic breast cancer (MBC): international expert consensus paper. Crit Rev Oncol Hematol 2019;134:39–45.
42. Yu M, Bardia A, Aceto N, Bersani F, Madden MW, Donaldson MC, et al. *Ex vivo* culture of circulating breast tumor cells for individualized testing of drug susceptibility. Science 2014;345:216–20.
43. Need EF, Selth LA, Harris TJ, Birrell SN, Tilley WD, Buchanan G. Research resource: interplay between the genomic and transcriptional networks of androgen receptor and estrogen receptor α in luminal breast cancer cells. Mol Endocrinol 2012;26:1941–52.
44. Creighton CJ, Cordero KE, Larios JM, Miller RS, Johnson MD, Chinnaiyan AM, et al. Genes regulated by estrogen in breast tumor cells in vitro are similarly regulated in vivoin tumor xenografts and human breast tumors. Genome Biol 2006;7:R28.
45. Li Z, Wu Y, Bahreini A, Priedigkeit NM, Ding K, Sartorius CA, et al. ESR1 mutant breast cancers show elevated basal cytokeratins and immune activation. bioRxiv; 2020.
46. Oyamada M, Takebe K, Oyamada Y. Regulation of connexin expression by transcription factors and epigenetic mechanisms. Biochim Biophys Acta 2013;1828:118–33.
47. Nigam A, Savage F, Boulos P, Stamp G, Liu D, Pignatelli M. Loss of cell-cell and cell-matrix adhesion molecules in colorectal cancer. Br J Cancer 1993;68:507–14.
48. Rege TA, Hagood JS. Thy-1 as a regulator of cell-cell and cell-matrix interactions in axon regeneration, apoptosis, adhesion, migration, cancer, and fibrosis. FASEB J 2006;20:1045–54.
49. Anania M, Sensi M, Radaelli E, Miranda C, Vizioli M, Pagliardini S, et al. TIMP3 regulates migration, invasion and *in vivo* tumorigenicity of thyroid tumor cells. Oncogene 2011;30:3011–23.
50. Su C-W, Chang Y-C, Chien M-H, Hsieh Y-H, Chen M-K, Lin C-W, et al. Loss of TIMP3 by promoter methylation of Sp1 binding site promotes oral cancer metastasis. Cell Death Dis 2019;10:793.
51. Zardavas D, Baselga J, Piccart M. Emerging targeted agents in metastatic breast cancer. Nat Rev Clin Oncol 2013;10:191–210.
52. Liu J, Pan S, Hsieh MH, Ng N, Sun F, Wang T, et al. Targeting Wnt-driven cancer through the inhibition of porcupine by LGK974. Proc Natl Acad Sci U S A 2013;110:20224–9.
53. Li Z, Levine KM, Bahreini A, Wang P, Chu D, Park BH, et al. Upregulation of IRS1 enhances IGF1 response in Y537S and D538G ESR1 mutant breast cancer cells. Endocrinology 2017;159:285–96.
54. Davis AA, Zhang Q, Gerratana L, Shah AN, Zhan Y, Qiang W, et al. Association of a novel circulating tumor DNA next-generating sequencing platform with circulating tumor cells (CTCs) and CTC clusters in metastatic breast cancer. Breast Cancer Res 2019;21:137.
55. Gerratana L, Davis AA, Polano M, Zhang Q, Shah AN, Lin C, et al. Understanding the organ tropism of metastatic breast cancer through the combination of liquid biopsy tools. Eur J Cancer 2021;143:147–57.
56. Aasen T, Mesnil M, Naus CC, Lampe PD, Laird DW. Gap junctions and cancer: communicating for 50 years. Nat Rev Cancer 2016;16:775–88.
57. Xu X, Wang J, Han K, Li S, Xu F, Yang Y. Antimalarial drug mefloquine inhibits nuclear factor kappa B signaling and induces apoptosis in colorectal cancer cells. Cancer Sci 2018;109:1220–9.
58. Simpson KJ, Selfors LM, Bui J, Reynolds A, Leake D, Khvorova A, et al. Identification of genes that regulate epithelial cell migration using an siRNA screening approach. Nat Cell Biol 2008;10:1027–38.
59. Björklund P, Svedlund J, Olsson A-K, Åkerström G, Westin G. The internally truncated LRP5 receptor presents a therapeutic target in breast cancer. PLoS One 2009;4:e4243.
60. O'Leary B, Cutts RJ, Liu Y, Hrebien S, Huang X, Fenwick K, et al. The genetic landscape and clonal evolution of breast cancer resistance to palbociclib plus fulvestrant in the PALOMA-3 trial. Cancer Discov 2018;8:1390–403.
61. Zundelevich A, Dadiani M, Kahana-Edwin S, Itay A, Sella T, Gadot M, et al. ESR1 mutations are frequent in newly diagnosed metastatic and loco-regional recurrence of endocrine-treated breast cancer and carry worse prognosis. Breast Cancer Res 2020;22:16.
62. Theodorou V, Stark R, Menon S, Carroll JS. GATA3 acts upstream of FOXA1 in mediating ESR1 binding by shaping enhancer accessibility. Genome Res 2013;23:12–22.
63. Xhabija B, Kidder BL. KDM5B is a master regulator of the H3K4-methylome in stem cells, development and cancer. Semin Cancer Biol 2019;57:79–85.
64. Williams MM, Spoelstra NS, Arnesen S, O'Neill KI, Christenson JL, Reese J, et al. Steroid hormone receptor and infiltrating immune cell status reveals therapeutic vulnerabilities of ESR1 mutant breast cancer. Cancer Res 2021;81:732–46.